

The dynamic floor of Yellowstone Lake, Wyoming, USA: The last 14 k.y. of hydrothermal explosions, venting, doming, and faulting

L.A. Morgan^{1,†}, W.C.P. Shanks¹, K.L. Pierce^{2,§}, N. Iverson³, C.M. Schiller^{4,#}, S.R. Brown^{5*}, P. Zahajska⁶, R. Cartier⁶, R.W. Cash⁷, J.L. Best^{7,8}, C. Whitlock⁴, S. Fritz⁵, W. Benzel⁹, H. Lowers⁹, D.A. Lovalvo¹⁰, and J.M. Licciardi¹¹

"This doubtless mere fragment of an ancient inland sea, or great lake, of perhaps hot or tepid water, surrounded and dotted by active volcanoes, has been so long, and yet so imperfectly known, and in trapper legends has been presented in so many different localities, shapes, dimensions, elevations, etc., that it appropriately merits its designation of "Mystic Lake." It has, however, been found to be one of the largest, most elevated, and peculiarly formed of all the mountain lakes of North America, and yet is comparatively so little known as to offer a most inviting field for romantic and interesting exploration."

—Superintendent Philetus W. Norris, Annual Report of the Superintendent of the Yellowstone National Park, 1881, p. 11, (Norris, 1881).

ABSTRACT

Hydrothermal explosions are significant potential hazards in Yellowstone National Park, Wyoming, USA. The northern Yellowstone Lake area hosts the three largest hydrothermal explosion craters known on Earth empowered by the highest heat flow values in Yellowstone and active seismicity and deformation. Geological and geochemical studies of eighteen sublacustrine cores provide the first detailed synthesis of the age, sedimentary facies, and origin of multiple hydrothermal explosion deposits.

L.A. Morgan https://orcid.org/0000-0002-5460-8754

New tephrochronology and radiocarbon results provide a four-dimensional view of recent geologic activity since recession at ca. 15–14.5 ka of the >1-km-thick Pinedale ice sheet.

The sedimentary record in Yellowstone Lake contains multiple hydrothermal explosion deposits ranging in age from ca. 13 ka to ~1860 CE. Hydrothermal explosions require a sudden drop in pressure resulting in rapid expansion of high-temperature fluids causing fragmentation, ejection, and crater formation; explosions may be initiated by seismicity, faulting, deformation, or rapid lake-level changes. Fallout and transport of ejecta produces distinct facies of subaqueous hydrothermal explosion deposits. Yellowstone hydrothermal systems are characterized by alkaline-Cl and/or vapor-dominated fluids that, respectively, produce alteration dominated by silica-smectite-chlorite or by kaolinite. Alkaline-Cl liquids flash to steam during hydrothermal explosions, producing much more energetic events than simple vapor expansion in vapor-dominated systems. Two enormous explosion events in Yellowstone Lake were triggered quite differently: Elliott's Crater explosion resulted from a major seismic event (8 ka) that ruptured an impervious hydrothermal dome, whereas the Mary Bay explosion (13 ka) was triggered by a sudden drop in lake level stimulated by a seismic event, tsunami, and outlet channel erosion.

INTRODUCTION

Hydrothermal explosions, unrelated to magmatic eruptions, have emerged as one of the most important and least understood geologic hazards in Yellowstone National Park (YNP), Wyoming, USA, and similar volcanic and hydrothermal areas worldwide (Browne and Lawless, 2001; Christiansen et al., 2007; D'Elia et al., 2020; Lowenstern et al., 2005; Montanaro et al., 2016a, 2016b, 2020a, 2020b). The

GSA Bulletin; March/April 2023; v. 135; no. 3/4; p. 547–574; https://doi.org/10.1130/B36190.1; 18 figures; 2 tables; 1 supplemental file. published online 7 June 2022

¹U.S. Geological Survey, Yellowstone Volcano Observatory, Denver, Colorado 80225-0046, USA

²U.S. Geological Survey, Rocky Mountain Science Center, Bozeman, Montana 59715, USA

³New Mexico Institute of Mining and Technology, New Mexico Bureau of Geology and Mineral Resources, Socorro, New Mexico 87801, USA

⁴Montana State University, Department of Earth Sciences, Bozeman, Montana 59717, USA

⁵University of Nebraska-Lincoln, Department of Earth and Atmospheric Sciences, Lincoln, Nebraska 68588-0340 USA

⁶Lund University, Department of Geology, Lund, 22362, Sweden

⁷University of Illinois at Urbana-Champaign, Department of Geology, Urbana, Illinois 61801, USA

⁸University of Illinois at Urbana-Champaign, Departments of Geography and GIS, Mechanical Science and Engineering and Ven Te Chow Hydrosystems Laboratory, Urbana, Illinois 61801, USA

⁹U.S. Geological Survey, Geology, Geophysics, and Geochemistry Science Center, Denver, Colorado 80225-0046, USA

¹⁰The Global Foundation for Ocean Exploration, Mystic, Connecticut 06355, USA

¹¹Department of Earth Sciences, University of New Hampshire, Durham, New Hampshire 03824, USA

[†]lmorgan@usgs.gov.

[§]Deceased.

^{*}Present address: Department of Biology, University of Washington, Seattle, Washington 98195, USA.

^{*}Present address: Division of Natural Science, Applied Science, and Mathematics, Defiance College, Defiance, Ohio 43512, USA.

northern Yellowstone Lake area is characterized by a combination of high heat flow above a large magma reservoir in the collapsed 631 k.y. Yellowstone Caldera (Favorito et al., 2021; Morgan et al., 1977; Smith et al., 2009; Sohn et al., 2019), active seismicity and deformation (Dzurisin et al., 2012; Farrell et al., 2014), and the presence of hundreds of hydrothermal features including vents, explosion craters, and domes (Johnson et al., 2003; Morgan et al., 2003, 2007a, 2007b, 2009). The area is particularly hazardous with respect to potential hydrothermal explosions and is an ideal natural laboratory for detailed research into hydrothermal explosion processes, timing, and triggering mechanisms.

A sediment-coring campaign was conducted in Yellowstone Lake to better understand the frequency, distribution, processes, and causes of hydrothermal explosions over the last ~ 14 k.y. Remarkably, subaqueous hydrothermal explosion deposits in the sedimentary record are largely unrecognized and their characteristics are fundamentally unknown. Our findings provide a basis for understanding hydrothermal explosion deposits in subaqueous sedimentary sequences and supplement recent and ongoing integrated research on hydrothermal fluid systems venting on the lake floor, inferred at temperatures >220 °C at relatively shallow depths (Balistrieri et al., 2007; Fowler et al., 2019a, 2019b; Favorito et al., 2021; Morgan et al., 2003, 2009; Shanks et al., 2005, 2007; Sohn et al., 2019).

The northeastern area of Yellowstone Lake has an abundance of large (500-2500 m diameter) explosion craters (Fig. 1), more concentrated than anywhere in YNP (Lowenstern et al., 2005). Located here are the partially submerged 13 ka Mary Bay explosion crater (2.5 km diameter), the subaerial 9.4 ka Turbid Lake explosion crater (1.6 km diameter), the sublacustrine 8 ka Elliott's Crater (>700 m diameter), and the subaerial 2.9 ka Indian Pond explosion crater (~500 m diameter) (Morgan et al., 2003, 2007a, 2007b, 2009; Muffler et al., 1971; Pierce et al., 2007; Wold et al., 1977) (Note: ka = 1000 years before 1950 CE). Subaerial deposits of explosion breccia around the craters are distinct in clast lithologies that reflect the subsurface geology below the crater (Morgan et al., 2009).

As part of the recent (2016–2019) multidisciplinary project "Hydrothermal Dynamics of Yellowstone Lake" (https://hdylake .org), coring enabled the identification and mapping of known and previously unknown hydrothermal explosion deposits in the lake basin and allowed documentation of past hydrothermal activity in Yellowstone Lake (Table S1¹). In this paper, we decipher the hydrothermal history of Yellowstone Lake during the past 14 k.y. with a focus on hydrothermal explosion events. Previous studies demonstrate that a thick (up to ∼100 m) sequence of lacustrine and glaciolacustrine sediments are in the northern lake (Otis et al., 1977) that overlie a series of post-caldera rhyolitic lava flows, many of which are exposed in bluffs to the west and north of the lake (Finn and Morgan, 2002; Morgan et al., 2003, 2007a, 2007b; Richmond, 1973, 1976, 1977). The 631 k.y. Lava Creek Tuff and Tertiary volcanic rocks are exposed outside the caldera margin, east of the lake (Christiansen, 2001).

We define six facies of subaqueous hydrothermal explosion deposits that allow identification of emplacement processes in proximal and distal depositional environments and will guide future studies of subaqueous hydrothermal explosion deposits. Integrated lithological, mineralogical, and geochemical studies facilitate recognition of the explosion deposits and allow interpretation of pre-explosion hydrothermal alteration conditions. Two distinct types of hydrothermal systems produce hydrothermal explosions in Yellowstone Lake: (1) neutral to alkaline pH, NaCl-rich (hereafter referred to as "alkaline-Cl") liquids that flash to steam under decompression producing the largest explosions in terms of energy, volume, and crater size, and (2) vapor-expansion explosions in vapor-dominated (steam-CO₂-H₂S) systems that produce smaller, possibly more frequent, events. We provide evidence that triggering mechanisms for the larger explosion events are related to seismicity and faulting, deformation, and sudden lake-level changes. We suggest that a general relationship between the composition of hydrothermal fluids and the magnitude of explosions produced is critical in assessing the potential hazard of future hydrothermal explosions.

FIELD METHODS

Coring sites in 2016 in northern Yellowstone Lake were selected using previous high-resolution multibeam bathymetry, seismic-reflection profiling, aeromagnetic data, and geologic mapping to target active geologic and hydrothermal areas (Cash, 2015; Finn and Morgan, 2002; Johnson et al., 2003; Morgan et al., 2003, 2007a). Using the Continental Scientific Drilling (CSD) Facility, University of Minnesota (Twin Cities, Minnesota, USA), eight 4- to 12-m-long sediment cores were collected from six sites using a Kullenberg piston coring system (Kelts et al., 1986). These include sediment cores from: (1) a hydrothermal dome (YL16-1A); (2) inside the western fault of the active Lake Hotel graben (YL16-2A, YL16-2C); (3) the active Deep Hole hydrothermal vent field in the lake's deepest region (≥119 m depth) (YL16-3A); (4) the floor of Elliott's Crater, a long-lived hydrothermally active explosion crater (YL16-4A, YL16-4C); (5) the deep central basin (YL16-5A); and (6) a steep-sloped shoreline prone to slumping activity (YL16-6A) (Table S1; Figs. 1-3).

Four 7- to 9-m-long sediment cores, collected in 1992 from three sites in Yellowstone Lake and stored under refrigeration at the CSD Facility, were re-examined and analyzed as part of this study to supplement the 2016 cores. The 1992 sediment cores came from between Frank and Dot islands in the south-central lake (YL92-1A, YL92-1C), South Arm (YL92-2A), and West Thumb basin (YL92-3A) (Table S1; Fig. 1). Two cores, collected in 2017 from the fen wetlands around Cub Creek Pond, 4 km east of northern Yellowstone Lake, also were examined (Y17-CUB-1A, Y17-CUB-1B). A description of a sediment core collected in Alder Lake in 1988 also was considered (Tiller, 1995; Sherrod, 1989), although this core is no longer available for examination. Finally, three additional short cores collected in 2016 and 2017 from the R/V Annie using a 1.6-m-long gravity corer were examined. In total, 18 cores were studied.

LABORATORY METHODS

Sediment cores were scanned for gamma density, acoustic velocity, electrical resistivity, and natural gamma radiation within their sealed polycarbonate core liners. After splitting, the cores were scanned for magnetic susceptibility and high-resolution digital images. Split cores also were analyzed for elemental variations at the University of Minnesota Duluth-Large Lakes Observatory using an ITRAX X-ray fluorescence (XRF) scanner. Results are semiquantitative because of variations in sediment matrix and reported as relative variations in counts for a particular element per interval.

Each core was described and smear slides were prepared for petrographic analysis at 1–10 cm intervals throughout the cores but with

¹Supplemental Material. Table S1: Coring locations, site data, and geologic environment. Table S2: Chemical data from electron microprobe analyses of glass grains from Yellowstone tephra samples and from established standard samples of Mazama tephra, Glacier Peak tephra, and Yellowstone rhyolites. Table S3: Characteristics of limnic facies in sediments from Yellowstone Lake, Wyoming, USA, modified after Tiller (1995). Table S4: Estimates of deposit volumes from Mary Bay and Elliott's Crater hydrothermal explosions and energy produced. Please visit https://doi.org/10.1130/GSAB.S.19497224 to access the supplemental material, and contact editing@geosociety. org with any questions.

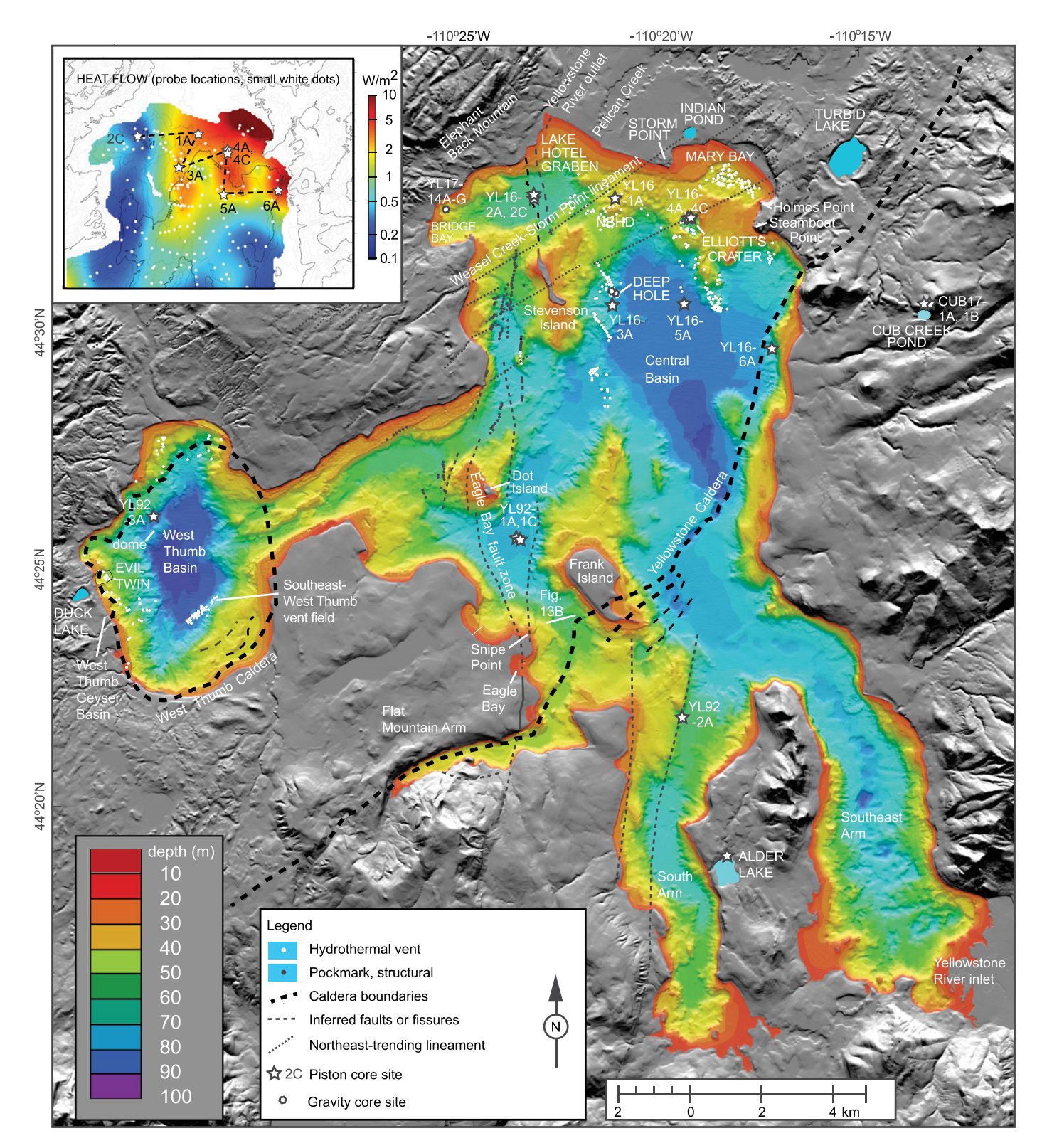


Figure 1. Color-shaded bathymetric map of Yellowstone Lake, Wyoming, USA (Morgan et al., 2007a) showing locations of cores used in this study relative to major tectonic features (faults, fractures, lineaments, caldera margins) and hydrothermal areas (vents, domes, hydrothermal explosion craters). Indian Pond, Turbid Lake, Mary Bay, Elliott's Crater, Duck Lake, and Evil Twin are large hydrothermal explosion craters. North Basin Hydrothermal Dome (NBHD) and Storm Point are large hydrothermal domes. Inset: Heat-flow map of northern Yellowstone Lake (Bouligand et al., 2020) defines areas of most intense hydrothermal activity and shallowest Curie temperatures due to a shallow magma chamber depth beneath the Yellowstone Caldera. Modified after Smith et al. (2009). The dashed black line represents the cross section through the locations of the 2016 piston cores shown in Figure 2.

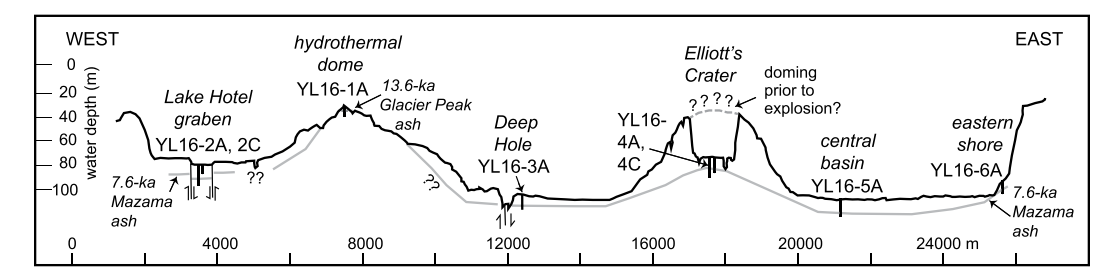


Figure 2. West-to-east crossbasin bathymetric profile of YL16 piston core locations in northern Yellowstone Lake, Wyoming, USA (cross-section location shown in Fig. 1 inset). Profile shows structural setting of Lake Hotel graben, the Deep Hole, selected hydrothermal domal features in the north

lake, the Elliott's Crater large hydrothermal explosion crater with inferred hydrothermal doming prior to explosion, and the eastern shore slump area. The 8 ka Elliott's Crater explosion deposits and the 7.6 ka Mazama tephra (light gray line) are found in cores YL16-2C, YL16-3A, YL16-4A, YL16-4C, YL16-5A, and YL16-6A (represented as vertical black lines). The 13 ka Mary Bay hydrothermal explosion deposits and the 13.6 ka Glacier Peak tephra occur on the hydrothermal dome in YL16-1A; both deposits are at shallower-than-expected depths due to sloughing of lake sediments off the top of the dome as it uplifted.

an emphasis on more detailed description of the distinct, hydrothermally altered sedimentary sequences. Each smear slide was examined under a polarizing microscope for grain size, mineralogy, limnic biota, and texture.

Age determinations were obtained by radiocarbon analyses (Table 1) and identification of known tephra layers (Table S2). Fifteen samples of terrestrial plant macrofossils and charcoal particles were analyzed by accelerator mass spectrometry (AMS) for radiocarbon age at the National Ocean Sciences AMS facility at Woods Hole Oceanographic Institute, Massachusetts, USA. Tephra samples were characterized and analyzed at the New Mexico Bureau of Geology and Mineral Resources Microprobe Lab (New Mexico, USA) using single-grain microprobe analyses.

Whole-rock and clay-fraction mineralogy was determined by X-ray Diffraction (XRD) analysis at the U.S. Geological Survey-Denver (Colorado, USA) using a PANalytical X'Pert PRO MPD X-ray diffractometer. Scanning Electron Microscopy (SEM) micro-imaging with Energy Dispersive Spectroscopy spot analysis for chemical constituents was conducted at the U.S. Geological Survey-Denver Microbeam Laboratory using a FEI Quanta 450 field emission gun—SEM and an Oxford Instruments Max 50 silicon drift detector.

RESULTS

Core Characteristics

Sediment cores collected from Yellowstone Lake have as many as ten limnic facies (Table S3) and contain interbedded hydrothermal explosion deposits and one or two thin tephra layers (Figs. 4A and 4B). Most of the cores contain either the 7.6 ka Mazama ash or the 13.6 ka Glacier Peak ash or both (Table S2). No tephra is identified in the three shorter cores (YL16-18A-1G, YL17-10A-1G, YL17-14A-1G) and core YL16-2A does not contain tephra or hydrothermal explosion deposits. The other longer cores contain

hydrothermal explosion deposits from either the Elliott's Crater or Mary Bay events; three of the longer cores and the three short cores also contain other hydrothermal explosion deposits. Many of the hydrothermal explosion sequences record multiple pulses of the explosion as evidenced by a series of normally graded sedimentary sequences, each sequence beginning with a sharp contact and abrupt changes in grain size; the sequences are repeated with each overlying one becoming gradually finer in grain size (Figs. 4A and 4B).

Sedimentation rates vary throughout Yellowstone Lake based on linear regression analyses using tephra and radiocarbon ages (Fig. 5). The sedimentation rates in the northern lake and West Thumb basin average \sim 1.06 m/k.y. based on data from cores YL16-3A, YL16-4A, YL16-4C, YL16-5A, and YL92-3A (Fig. 1). For the southern lake, rates average \sim 0.62 m/k.y. from cores YL92-1A, YL92-1C, and YL92-2A, consistent with the rate determined for YL92-1A by Theriot et al. (2006).

Geochemical analysis of the glass-bearing tephra samples reveals two distinct compositions of glass (Fig. 6A). The Mazama ash (7682–7584, 7633 avg. cal yr B.P.; Egan et al., 2015; Jensen and Beaudoin, 2016) is a low-silica rhyolite (~73 wt% SiO₂) whereas the Glacier Peak

Figure 3. Geologic, structural, and hydrothermal features of YL16 coring sites in northern Yellowstone Lake, Wyoming, USA, illustrated using high-resolution, color-shaded bathymetric maps with core locations (white stars or hexagons) and selected hydrothermal vent fluid samples sites (white or black dots) (Cash, 2015; Gemery-Hill, 2007; Morgan et al., 2003, 2007a), selected seismic-reflection profiles with core locations as red vertical lines (Johnson et al., 2003). (A) Core YL16-1A was collected on an inactive hydrothermal dome northeast of North Basin Hydrothermal Dome (NBHD), where low-Cl hydrothermal fluids have been sampled. The seismic-reflection profile shows a typical cross section of a hydrothermal dome; green lines represent reflectors. Seismic sequences I (glacial) and II (post-glacial) are from Johnson et al. (2003). (B) Cores YL16-2A and YL16-2C were collected in the western margin of the active Lake Hotel graben. Also shown is line A-A', the location of a seismic-reflection profile shown in Figure 13A. (C) Location of the Deep Hole hydrothermal vent area along the active northwest-trending fissure east of Stevenson Island showing locations of YL16-3A, YL16-18A-1G, YL17-10A-1G, and sites where low-Cl fluids were collected. A'-A is a topographic profile cutting northeast across the Deep Hole, an active 200-m-wide hydrothermal vent area. B'-B is a seismic-reflection profile cutting south to north across the Deep Hole, highlighting the location of the active vent field, an active fault that has a 6.7-m offset along which fluids are ascending, and the approximate location of core YL16-3A. Doming of lacustrine sediments, seismic sequences I and II, and ascending hydrothermal fluids also are shown. (D) Elliott's Crater showing locations of YL16-4A, YL16-4C, and sites where low-Cl and high-Cl vent fluids were collected. Oblique color-shaded bathymetric map shows Elliott's Crater and a lobe of explosion breccia deposits to the south-southeast. Seismic-reflection profile A'-A across Elliott's Crater shows hydrothermal vents and layered near-surface lake sediments that are upwarped by hydrothermal doming. (E) Location of YL16-6A along the eastern shore of Yellowstone Lake showing the topographic margin of the Yellowstone Caldera and multiple mud slump lobes coming into the lake from the steep eastern shoreline. (F) Mary Bay crater showing the extent of the main crater and the deeper inner crater, and locations where low-Cl and high-Cl vent fluids were sampled. TWT-two-way travel time; VE-vertical exaggeration.

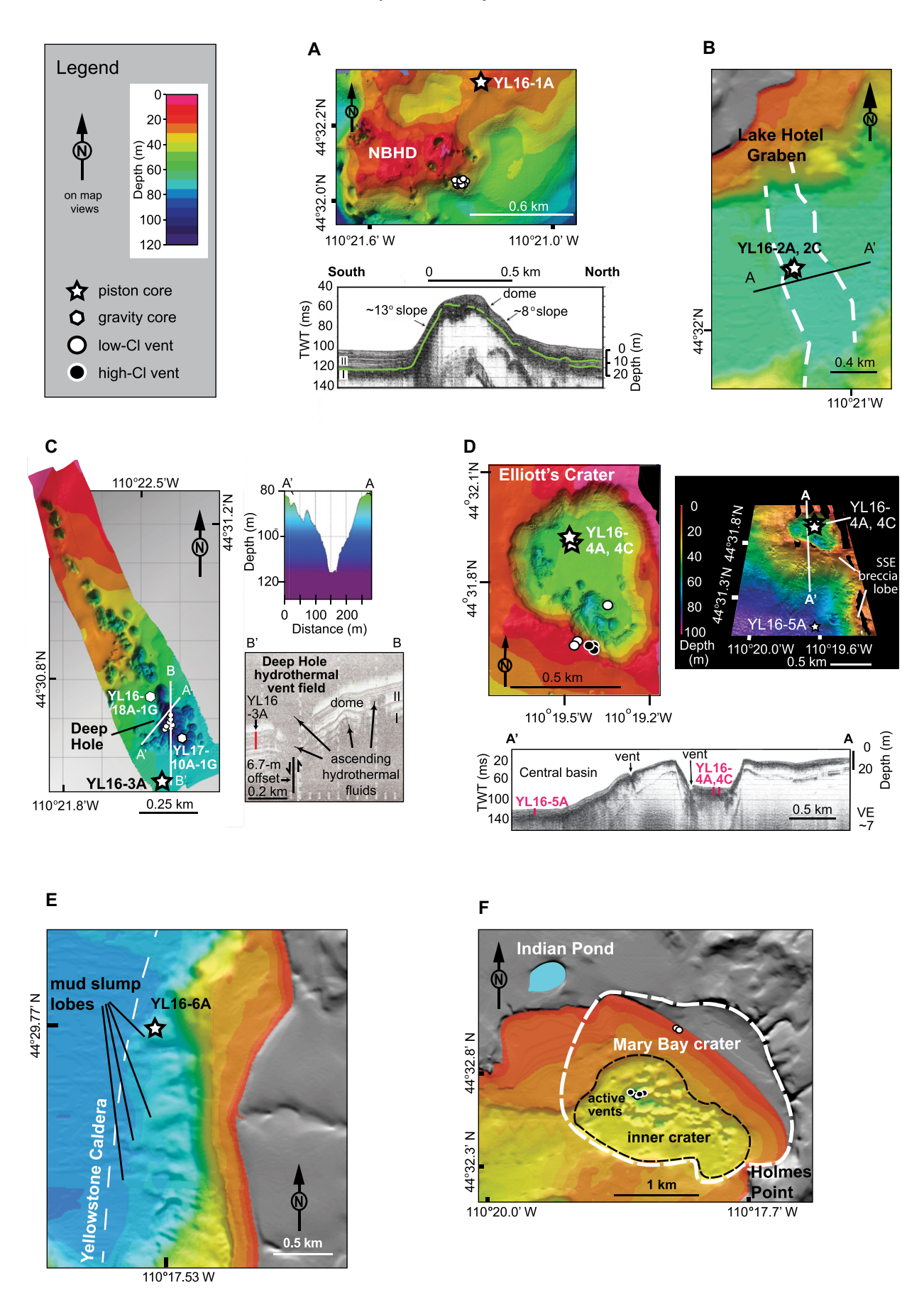


TABLE 1, RADIOCARBON AGE CONTROLS, YELLOWSTONE LAKE, WYOMING, USA

Accession no.	Core no.	Core depth (cm)	Section/depth (cm)	Material dated*	δ ¹³ C (‰ VPDB)	Age (¹⁴ C)	2σ calibrated age range (probability)†	Median calibrated age [†]
<u>YL16-2C</u> OS-135957	YL16-2C	328.0	3/131–133	Terrestrial plant	-26.33	2590 ± 20	2723–2754 (1.000)	2743
OS-135958	YL16-2C	400.0	4/71–72	fragment Wood	-27.97	3150 ± 25	3272–3285 (0.038),	3378
OS-136956	YL16-2C	621.5	6/3–4	Wood	N.D.	4510 ± 20	3339–3445 (0.962) 5053–5190 (0.688), 5213–5296 (0.312)	5156
OS-142084	YL16-2C	750.0	7/47–48	Aquatic plant fragment	-10.86	9980 ± 45	11259–11623 (0.985), 11675–11694 (0.015)	11434
OS-138622	YL16-2C	964.0	8/110.5	Wood	N.D.	5740 ± 30	6453–6459 (0.012), 6462–6634 (0.988)	6536
<u>YL16-3A</u> OS-142041	YL16-3A	823.0	8/84.5–86.3	Charcoal	-26.29	8140 ± 35	9003–9138 (0.927), 9174–9206 (0.041), 9217–9244 (0.032)	9073
OS-142090	YL16-3A	1012.7	10/1–2.2	Charcoal	N.D.	8080 ± 210	8478–8494 (0.006), 8514–9477 (0.994)	8980
<u>YL16-4C</u> OS-138623	YL16-4C	206.0	3/21.2	Wood	N.D.	2160 ± 20	2067–2081 (0.021), 2107–2181 (0.524), 2239–2303 (0.455)	2160
OS-138691	YL16-4C	436.0	4/101.6	Terrestrial plant fragment	N.D.	2600 ± 25	2721–2760 (1.000)	2746
<u>YL16-5A</u> OS-135959	YL16-5A	363.0	4/63.4	Charcoal	-27.08	3760 ± 30	3993–4039 (0.127), 4074–4184 (0.727), 4188–4192 (0.007), 4195–4235 (0.139)	4123
<u>YL16-6A</u> OS-138754	YL16-6A	254.0	3/90.6	Wood	N.D.	3340 ± 20	3484–3486 (0.003), 3494–3533 (0.119), 3554–3637 (0.878)	3582
OS-138755	YL16-6A	535.0	5/95–97.5	Wood	N.D.	5690 ± 25	6408–6531 (1.000)	6467
OS-138756	YL16-6A	718.5	7/21.9–22.4	Charcoal	N.D.	7770 ± 30	8455–8501 (0.153), 8506–8599 (0.847)	8556
<u>YL92</u> OS-154882	YL92-3A	357.0	4/62.3	Wood	N.D.	3300 ± 95	3344–3732 (0.963), 3744–3773 (0.015), 3789–3826 (0.022)	3540
OS-154761	YL92-3A	433.0	5/36.8–38	Charcoal	N.D.	$\textbf{3810} \pm \textbf{20}$	4098–4117 (0.039), 4146–4249 (0.950), 4274–4282 (0.011)	4196

*Suitably large, identifiably terrestrial plant remains were uncommon in most cores, but 12 samples of plant remains and charcoal were identified and submitted for accelerator mass spectrometry (AMS) radiocarbon age determinations. Radiocarbon samples were extracted from sediment, washed in distilled water, and cleaned with a teasing needle under a dissection microscope to remove extraneous sediment. Samples were pre-treated with a traditional acid-base-acid procedure (de Vries and Barendsen, 1954) to remove non-structural carbon. Age determinations were made by the National Ocean Sciences AMS facility at the Woods Hole Oceanographic Institute, Massachusetts, USA. AMS radiocarbon results were calibrated utilizing IntCAL13 (Reimer et al., 2013) and CALIB (version 7.1, Stuiver et al., 2020).

†Calibrated ranges calculated by CALIB; probability represents relative area under probability distribution of given calibrated age range; median calibrated ages rounded to nearest decade where radiocarbon error is >50 years. VPDB—Vienna Pee Dee belemnite; N.D.—no data.

ash (13,710-13,410; 13,560 avg. cal yr B.P.; Kuehn et al., 2009; Mehringer et al., 1977; Blinman et al., 1979) is a distinct, high-silica rhyolite (>77 wt% SiO₂). Glacier Peak produced multiple Plinian eruptions; the chemistry of the ash in Yellowstone Lake cores falls between those of Glacier Peak G and Glacier Peak B, which are chronologically indistinguishable (Kuehn et al., 2009). Additionally, the glass shards in each tephra have distinct morphologies: the Mazama shards are more pumiceous and finer grained with few shards longer than 100 µm; the Glacier Peak tephra has large, blocky, and vesiculated shards up to 200 µm (Fig. 6B). Ten sediment cores from Yellowstone Lake contain the Mazama ash, whereas five cores, including the two Cub Creek Pond cores, contain the Glacier Peak ash. Core YL92-1A and the Alder

Lake core (Sherrod, 1989; Tiller, 1995) contain both the Mazama and Glacier Peak tephra layers (Fig. 4B). A third glass composition also was noted in YL16-6A and appears to be a reworked Yellowstone volcaniclastic ash with \sim 78 wt% SiO₂ and lower CaO (\sim 0.5 wt%) and higher K₂O (\sim 5.0 wt%) than the Cascade tephras (Figs. 4A and 6A; Table S2).

Hydrothermal Explosion Facies and Related Deposits in Yellowstone Lake

Hydrothermal explosions are strictly related to aqueous fluids in areas of high heat flow and contain no primary magmatic material. They result in the fragmentation of rock by the phase transition of water to steam or by simple expansion of vapor. Hydrothermal explosions occur where near-boiling water is present and result from a sudden decrease in pressure causing the water to flash to steam, or in some instances, sudden vapor expansion with pressure release. Both processes result in significant volume expansion, large energy release, and fragmentation of the enclosing rocks often creating an explosion crater. Fragmented materials ejected from hydrothermal craters may have a broad range of clast sizes and compositions. On land, close to source, breccia typically is deposited as coarse, poorly sorted, primary fall material, refilling the explosion crater and creating a debris apron around and outside of the crater. Breccia lithologies reflect the shallow subsurface geology down to the maximum hydrothermal explosion excavation depth (Browne and Lawless, 2001). In the

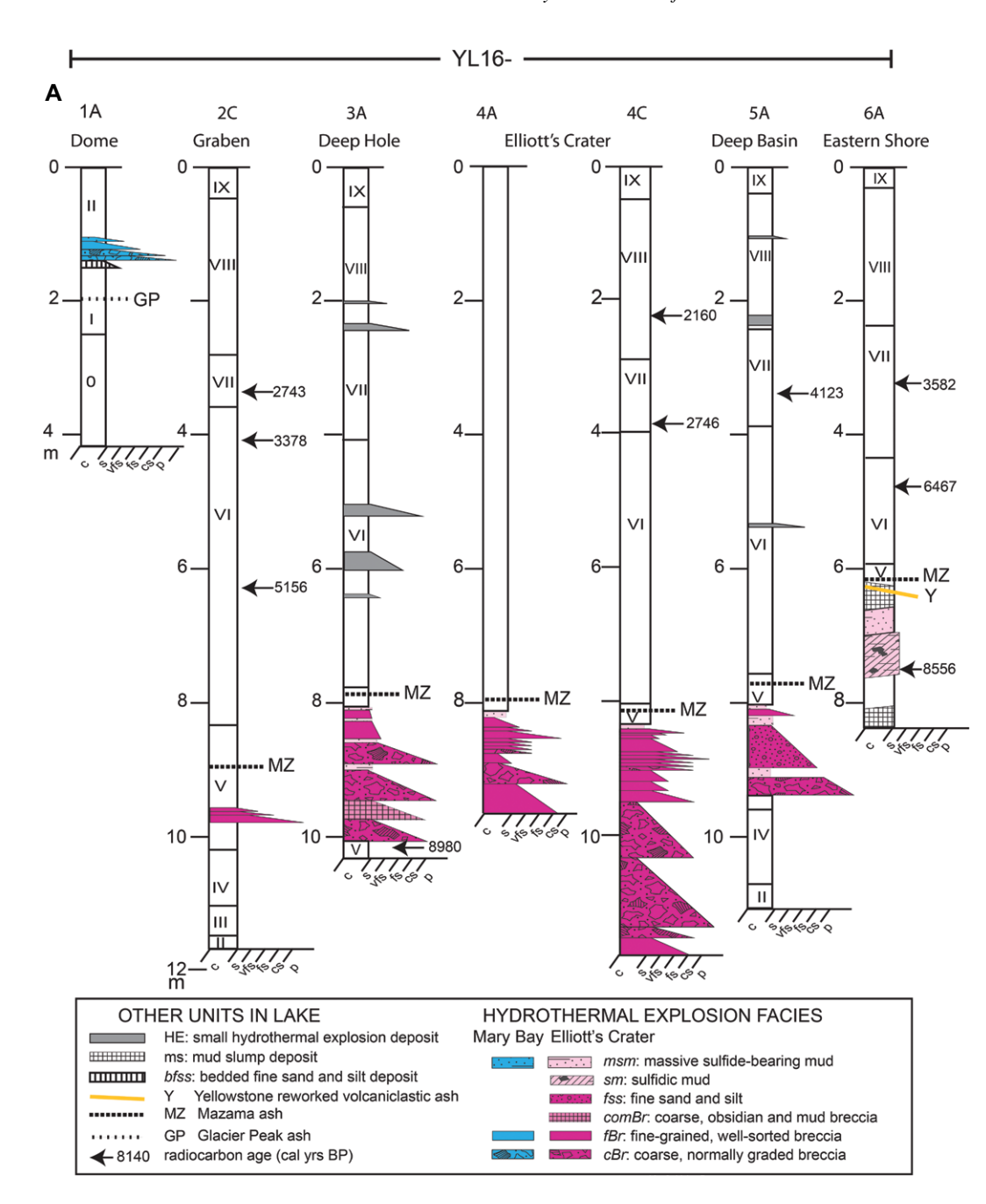


Figure 4. (A) Lithologic logs (depth vs. grain size) of 2016 piston cores collected from Yellowstone Lake, Wyoming, USA and (B) lithologic logs (depth vs. grain size) of 1992 piston cores collected from Yellowstone Lake (modified and reinterpreted from Tiller, 1995) and cores from Cub Creek Pond in 2017 (modified from Schiller et al., 2020). Also shown is simplified lithologic log of a core from Alder Lake, after Sherrod (1989) and Tiller (1995). Lithologies are subdivided into limnic facies (0-IX) (Table S3) and other units derived from volcanic ash, volcaniclastic layer, hydrothermal explosion deposits, tsunami-related bedded fine-grained sand-and-silt deposit, and mud slump deposits. Grain sizes of sediments: c-clay; s-silt; vfs-very fine sand; fs-fine sand; cs-coarse sand; p-pebble.

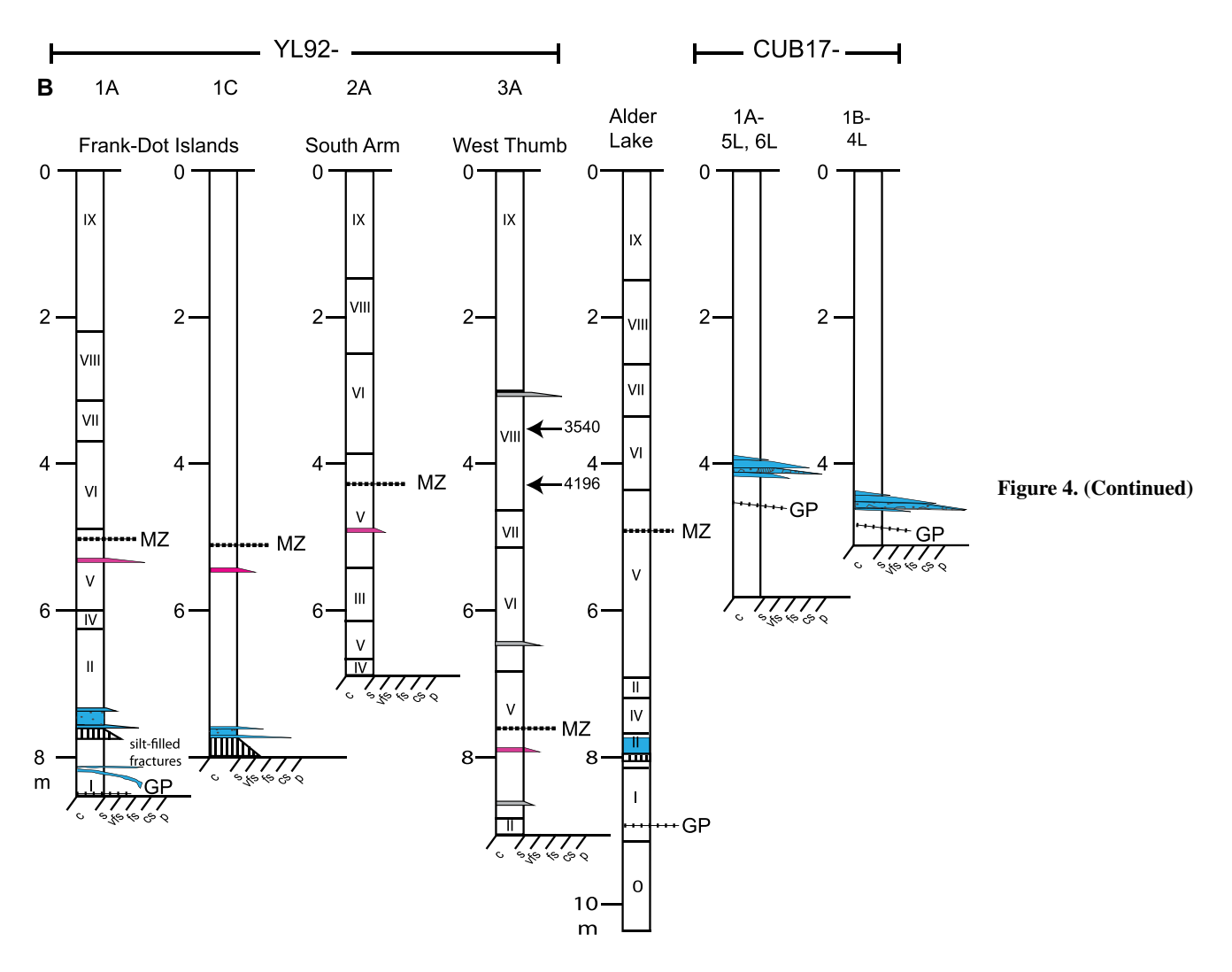
case of a subaqueous explosion, primary fall material is ejected and falls back through the water column where materials are physically sorted. Wave action, currents, and differential settling contribute to moving the ejecta and, as a result, explosion craters on the lake floor typically have subdued or nonexistent breccia rims around the crater.

The Yellowstone Lake cores contain deposits related to hydrothermal explosions that are distinct in lithology, alteration effects, sorting, grain size, and chemical and physical signatures from the lacustrine sediments in which they occur. Six subaqueous hydrother-

mal explosion facies are defined to provide a systematic classification that relates directly to processes of formation in proximal to distal settings (Table 2; Fig. 7). These include (1) proximal primary fall deposits (cBr), (2) distal or waning, fine-grained primary fall deposits (fBr), (3) proximal remobilized primary fall deposits (comBr), (4) fine-grained remobilized primary fall deposits (fss), (5) mud slump deposits (sm), and (6) suspension fallout deposits (msm). In addition, deposits interpreted as tsunami-related bedded fine sand and silt (bfss) underlie the Mary Bay explosion deposit.

Geochemical Signatures of Hydrothermal Explosion Deposits

Cores were scanned for selected major and trace elements. Scanning XRF analyses of Yellowstone Lake core sediments proved extremely useful for distinguishing unaltered lacustrine sediments from hydrothermally altered sequences and for identifying subtle variations among the explosion deposits (Fig. 8). Recurrent patterns in the hydrothermal explosion deposits show consistent depletion in As, enrichment in Sr and Si, and higher values of density and magnetic susceptibility relative to the lacustrine



sediments. Concentrations of Si are dependent on grain size: the finer the deposit, the greater the concentrations of Si.

The 2016 Yellowstone Lake Sediment Cores

Core YL16-1A: Top of a Hydrothermal Dome

Core YL16-1A was collected on a 400-mdiameter inactive hydrothermal dome having \sim 6-9 m of relief and an area of \sim 0.13 km² (Figs. 1, 2, and 3A). Three limnic facies are present (Fig. 4A, Table S3), including some of the oldest limnic facies known in the lake, which occur at surprisingly shallow depths at this location. Three significant deposits of various origin occur in the core: (1) at 2.0 m depth, the 13.6 ka Glacier Peak ash is a thin (0.1-0.2 cm) white tephra; (2) between 1.48 and 1.59 m depth, an 11-cm-thick, normally graded, bedded, fine sand-and-silt tsunami-related sequence (facies bfss), and (3) between 0.98 and 1.48 m depth, the 50-cm-thick, fining-upward (facies cBr, fBr, msm) Mary Bay hydrothermal explosion deposit (Fig. 4A). The deposits correlate with subaerial

exposures of the Mary Bay explosion deposit along the northern shore of Yellowstone Lake where the bedded sand-and-silt deposit (facies *bfss*) (Morgan et al., 2009) is below and in contact with the overlying, coarse, poorly sorted Mary Bay breccia. Radiocarbon ages of charcoal and insect fragments from exposures on land below the base of the Mary Bay deposit establish an age of ca. 13 ka for the explosion event (Pierce et al., 2007); additionally, the Mary Bay explosion breccia occurs above the 13.6 ka Glacier Peak ash in exposures on land and in the lake cores.

The Mary Bay explosion deposit in core YL16-1A includes several units that fine upward within an overall explosion sequence that is normally graded (Fig. 9A) and are indicative of deposition in a subaqueous environment. The explosion deposit has several internal contacts and is subdivided into four individual sequences (Figs. 4A and 8); most (facies *cBr* and *fBr*) contain dropstones (Bennett et al., 1996) at their base (Figs. 7A and 9A; Table 2). A fine-grained explosion breccia sample from 1.32 m depth

(Fig. 10A) contains abundant chlorite and smectite alteration and silica cementation.

Core YL16-2C: Inside the Active Lake Hotel Graben

Core YL16-2C was collected immediately east of the western fault within the active Lake Hotel graben (Figs. 1, 2, and 3B). Three major faulting events have occurred in the graben since its initial formation based on the offset of distinctive seismic reflectors (Johnson et al., 2003). The timing of the first graben-forming event is refined to 13 ka based on sedimentation rates determined in this study (Brown et al., 2021; Schiller et al., 2021).

Core YL16-2C contains eight limnic facies (II–IX, Table S3) and a 7-cm-thick (9.77 to 9.84 m depth), fining-upward sequence of the Elliott's Crater hydrothermal explosion deposit (Fig. 4A). At 9.34 m depth, the Mazama ash, a 4-mm-thick white tephra, is 43 cm above the Elliott's Crater explosion deposit.

The 7-cm-thick hydrothermal explosion sequence has three fine-grained, distal, fining-

¹⁴C calibrated k.y. BP

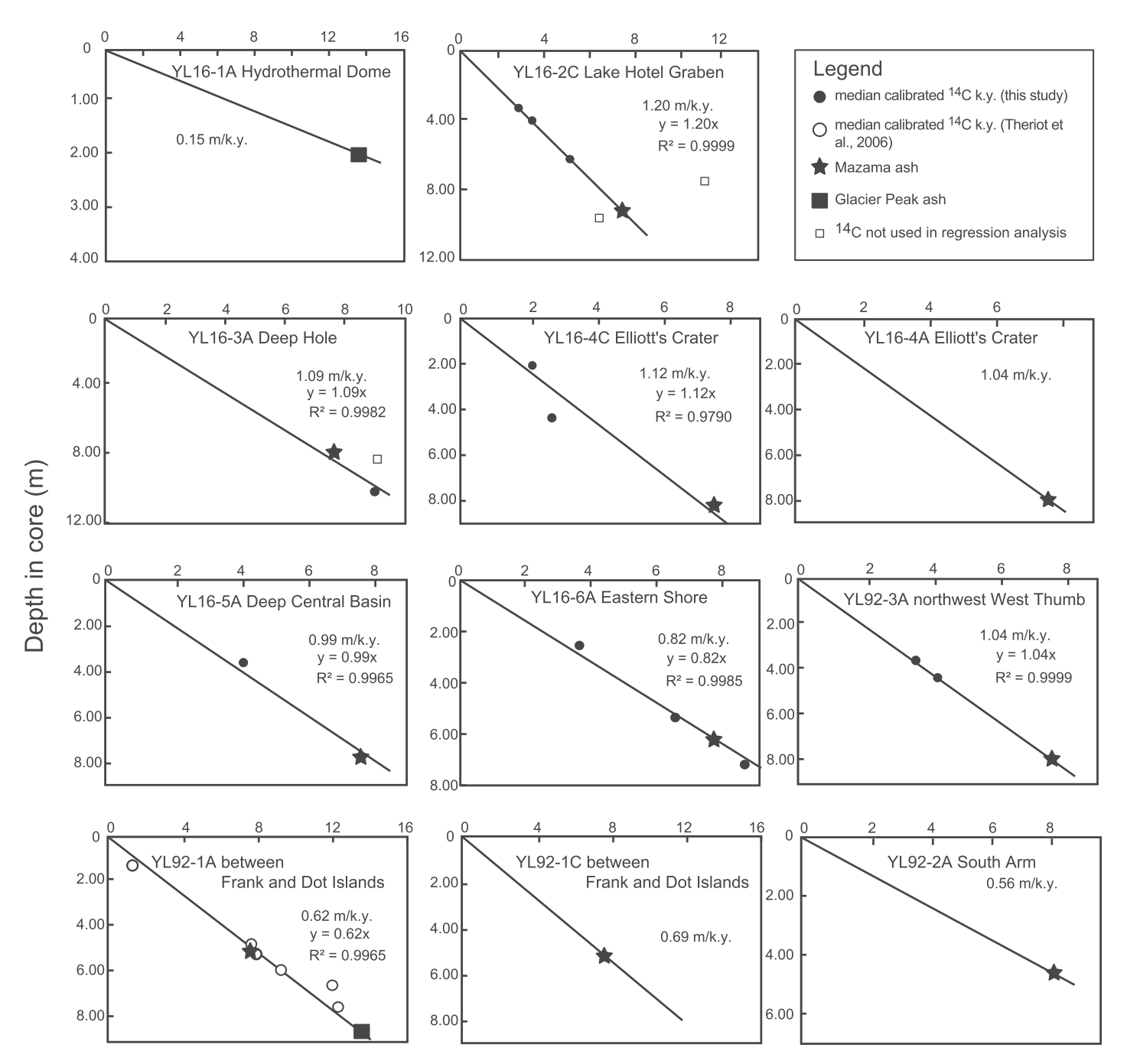
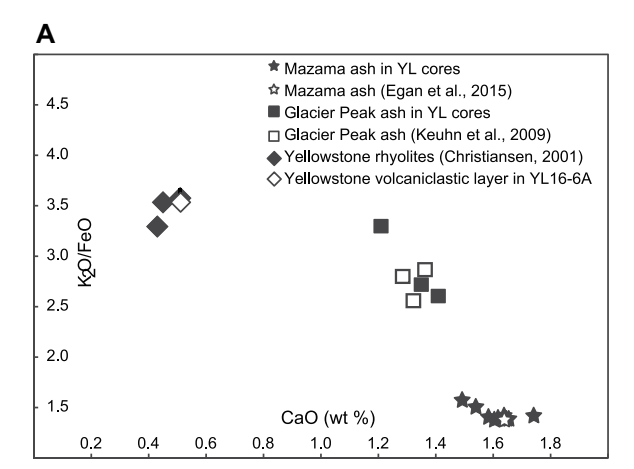


Figure 5. Plots of ¹⁴C calibrated age (k.y. B.P.) versus depth (m) in Yellowstone Lake, Wyoming, USA cores. Linear regression lines are based on ¹⁴C data (Table 1; Tiller, 1995; Theriot et al., 2006) and calibrated age of Mazama and Glacier Peak tephra deposits. Some ¹⁴C ages that deviate from the regression lines by more than two standard deviations relative to the other data are excluded from the regression analyses. Plots show range in sedimentation rates from 0.56 to 1.20 m/k.y.

upward sequences (Figs. 4A and 9B). The base of the explosion deposit in core YL16-2C has a sharp irregular contact with the underlying lake sediment and contains slightly larger (up to 6 mm, maximum diameter) fragments of

sinter and obsidian at the base (Fig. 9Ba). The basal contacts of the upper two sequences also contain slightly larger breccia fragments. The 7-cm-thick hydrothermal explosion sequence displays typical high values of magnetic sus-

ceptibility, As depletion, Sr enrichment, and Si enrichment in upper finer grained deposits (Fig. 8). A sample of predominantly unaltered lake sediment from limnic facies VI shows (Table S3; Fig. 10B) abundant diatoms and diatom



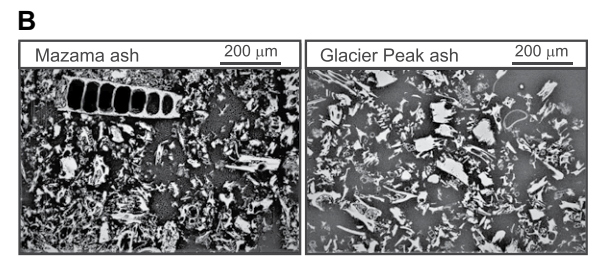


Figure 6. Chemical and mineralogical data used to identify tephra deposits from Yellowstone Lake, Wyoming, USA. (A) Plot of K₂O/FeO versus CaO for Mazama and Glacier Peak ashes and reworked volcaniclastic Yellowstone layer identified in cores and clearly discriminated by these and other element ratios. (B) Backscatter electron (BSE) images of tephra from Yellowstone Lake (YL) cores. Left: Representative BSE image of the Mazama ash in YL16-4C core with vesiculated pumice shards with cuspate margins. Right: Typical Glacier Peak ash in YL92-1A core with large blocky shards and a mix of vesiculated and non-vesiculated glass shards and an overall larger grain-size than in the Mazama ash. Freshwater diatoms are present in both samples.

fragments with minor amounts of barite, pyrite, and actinolite.

Core 3A: Near the Deep Hole, an Active Hydrothermal Vent Field

The Deep Hole (Fig. 3C) is located at the southern end of a prominent 1.4-km-long, northwest-trending fissure system containing over 61 crater-like large depressions (~50 to 300 m diameter) (Cash, 2015; Morgan et al., 2003; Sohn et al., 2017). The Deep Hole is the largest active hydrothermal vent field in this fissure system having some of the highest heat flow (Fig. 1 inset) and heat flux (~28 MW) values in Yellowstone Lake (Favorito et al., 2021; Sohn et al., 2019). A northeast-trending profile across the Deep Hole shows that the structure has high relief with V-shaped canyons as deep as 35-50 m and slopes up to 25° (Cash, 2015) (Fig. 3C). Johnson et al. (2003) mapped a southwest-northeast-trending fault in the Deep Hole with 6.7 m vertical displacement. This fault is active extending to the present surface of the lake floor (Fig. 3C) and likely is an important conduit supplying vapor-dominant

TABLE 2. DESCRIPTION AND INTERPRETATION OF FACIES IDENTIFIED IN SUBAQUEOUS HYDROTHERMAL EXPLOSION-RELATED DEPOSITS IN YELLOWSTONE LAKE, WYOMING, USA

Facies Lithology Interpretation Hydrothermal Explosion Deposits Coarse, fining-upward breccia facies: A coarse-grained (coarse pebble Proximal primary fall hydrothermal explosion deposit. Larger (<64 mm) to coarse sand (<2 mm)), light- to dark-colored, polymictic, rock fragments at base are interpreted as dropstones (Bennett normally graded, clast- to matrix-supported unit. Clasts are rounded to et al., 1996) related to the first coarse fragments deposited (D'Elia subangular and composition includes altered rhyolite, fractured obsidian, et al., 2020) through the water column onto underlying material sinter, and brown muds with sinter, subangular glass and broken crystals and represent projectiles associated with hydrothermal explosions of quartz, feldspar, and actinolite, commonly mantled with secondary occurring in a high-energy environment. Multiple sequences, hydrothermal quartz. Clasts may be coated with diatomaceous ooze, clay, representing different pulses in the explosion, may be present in and mud and are variably porous; all are hydrothermally altered. This unit is one stratigraphic package. typically the basal unit in a sequence of hydrothermally altered units although multiple cBr facies may be present. Typically, larger clasts at the base can extend into the underlying unit.

Fine-grained, well-sorted, fining-upward breccia facies: A fine (medium sand Distal or waning primary fall hydrothermal explosion deposit. fBr to clay), light- to dark-colored, polymictic, well-sorted, normally graded, clast-The distal, waning, or fine-grained equivalent to facies cBr. supported breccia. Clasts typically are rounded to subangular and similar in Multiple sequences, representing different pulses in the explosion, composition to the facies cBr; all are hydrothermally altered. Facies fBr may may be present in one stratigraphic package. contain larger clasts at base. Coarse, obsidian sand and mud breccia facies: A chaotic mix of coarse Proximal remobilized primary fall hydrothermal explosion comBi blocks of lake mud and large pockets of coarse obsidian sand; larger clasts of deposit. Deposited initially as a coarse ballistic hydrothermal explosion deposit in areas of high relief adjacent to steep slopes, angular to rounded hydrothermally altered debris also may be included. The facies has a non-planar or erosive base cut into the lower sequence. the deposit is inferred to have been quickly remobilized and redeposited. Fine sand-and-silt facies: A fining-upward, well-sorted fine sand grading Fine-grained remobilized primary fall hydrothermal explosion fss upward to silt and sometimes clay. Upward in the sequence are elongate, deposit. A fine-grained equivalent to facies comBr that collapsed subhorizontal feathery clasts of fine sand. The unit typically has an erosive from an area of high relief and was transported downslope and base cut into the lower sequence. redeposited to a stable area during rapid depositional events Sulfidic mud facies: A hydrothermally altered mud with black sulfidic streaks Mud slump deposit. A sulfidic mud slump deposit that incorporated or discontinuous splotches. Ranges from massive to clastic with large hydrothermal explosion-related materials with lacustrine intermingled randomly oriented clasts of mud with sulfidic streaks and, in sediments during mass wasting events. The physical and specific horizons, containing large angular clasts of white clay and wood chemical signatures of facies sm are somewhat muted compared to those observed in the primary fall and remobilized facies and distinct from lacustrine sediments (Fig. 8). Massive sulfide-bearing mud facies: A hydrothermally altered structureless Suspension fallout deposit. Represents fine-grained, msm mud with massive or weakly developed beds or laminations; some have hydrothermally altered, explosion debris suspended in the water column mixed with lacustrine detrital and biotic material during sulfidic streaks. May be bioturbated in upper part. The deposits have somewhat muted physical and chemical hydrothermal explosion signatures with chemical affinities similar to hydrothermal explosion deposits. Tsunami-related Deposits Bedded fine sand-and-silt facies: A medium grayish-brown, obsidian-bearing, Tsunami-related deposit. A lacustrine-equivalent deposit to a bedded unit that grades upward into a series of parallel, thin (1-2 mm) beds tsunami deposit (Morgan et al., 2009). Material was suspended in of concentrated black obsidian-rich fine sand alternating with finer silt. the water column eventually settling on the lake floor.

A Primary fall hydrothermal explosion deposits (facies cBr and fBr)

B Remobilized hydrothermal explosion deposit (facies comBr and fss)

msm

fss

52

53

55

58

C Explosion debris incorporated in mud slump deposits (facies sm)

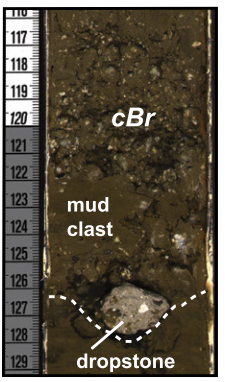
chlorite¹rich

sm

clasts

clay

D Suspension fallout deposit (facies msm)



YL16-5A: 9.25-9.38 m base of Elliott's Crater deposit

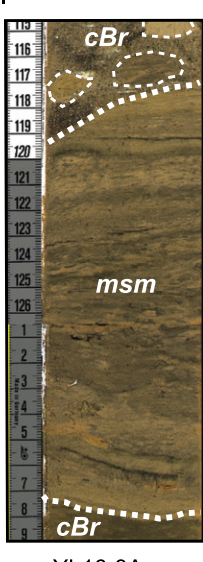


59

YL16-5A: 8.57-8.74 m Elliott's Crater deposit YL16-4C: 11.23 -11.45 m



black sulfidio streaks sm clasts of chlorite-rich 'clay sm



YL16-3A: 8.52-8.72 m Elliott's Crater deposit



YL16-1A: 1.38-1.49 m base of Mary Bay deposit



Elliott's Crater intracrater

deposit

YL16-2C: 9.80-9.85 m base of Elliott's Crater deposit

YL16-3A: 9.43-9.76 m Elliott's Crater deposit

YL16-6A: 7.10-7.43 m mud slump deposit with incorporated chlorite-rich clasts from Elliott's Crater explosion deposit

Figure 7. Images of six facies of sublacustrine hydrothermal explosion deposits in Yellowstone Lake, Wyoming, USA. Table 2 describes facies characteristics in more detail. Locations of cores and distances from Elliott's Crater and Mary Bay crater are in Table S1. (A) Examples of primary fall hydrothermal explosion deposits (facies cBr and fBr). (B) Examples of remobilized hydrothermal explosion deposit (facies comBr and fss). (C) Example of explosion debris incorporated into mud slump deposit (facies sm). (D) Example of suspension fallout deposit (facies msm).

fluids to the Deep Hole hydrothermal vents sampled (Fowler et al., 2019a).

Core YL16-3A, collected ~200 m south of the 200-m-wide active Deep Hole hydrothermal vent field (Figs. 1, 2, and 3C), has five limnic facies (Table S3) and six distinct hydrothermal explosion deposits (Fig. 4A). The Elliott's Crater explosion deposit (8.13 to 10.04 m depth; 1.92 m thick) occurs 27 cm below the 5-mmthick Mazama ash (7.86 m depth) and is the lowest explosion sequence in core YL16-3A (Fig. 4A).

The Elliott's Crater explosion deposit has multiple units based on chemical and physical characteristics (Figs. 4A, 8, 9Bc, and 9Bd) and is more complex than the Elliott's Crater sequences present in other cores. The base of the explosion deposit contains fining-upward interlayered

deposits of dark obsidian sands grading upward to altered muds (facies cBr), that grade upward into a series of disturbed deposits (facies com-Br), interpreted as proximal remobilized primary fall hydrothermal explosion deposits (Table 2; Figs. 7B and 8). The *comBr* facies deposits contain vertical or curved contacts with mud, zones of layered sediments with curved and dipping beds, and randomly distributed angular or rounded mud fragments of white or tan hydrothermally altered clay. A hydrothermally altered, white, angular mud clast at 8.80 m depth contains diatom fragments in a fine silica-cemented matrix, with a large anhydrite crystal, quartz, feldspars, clays (chlorite, smectite, illite), and framboidal pyrite masses (Figs. 10C and 10D). XRD analysis of the clay fraction shows major amounts of chlorite and minor illite.

Petrographic studies reveal the presence of quartz crystals with opaque inclusions (pyrite?), zoned plagioclase crystals, and masses of framboidal pyrite, all with a mantle of drusy quartz (Figs. 11A, 11B, and 11C). Pieces of broken, flow-banded rhyolite glass and broken glass shards in a diatomaceous, fine-grained groundmass are abundant in the deposit (Figs. 11D and 11E). Fresh, unbroken, segmented diatoms (Fig. 11F) were introduced from the water column during sedimentation.

Five thinner but notable explosion deposits interbedded in the lake sediments occur above the Mazama ash at 6.41-6.48 m (7 cm thick), 5.76-6.10 m (34 cm thick), 5.02-5.24 m (22 cm thick), 2.35-2.44 m (9 cm thick), and 2.04-2.06 m (2 cm thick) depth (Figs. 4A and 8). All are normally graded sequences interpreted as

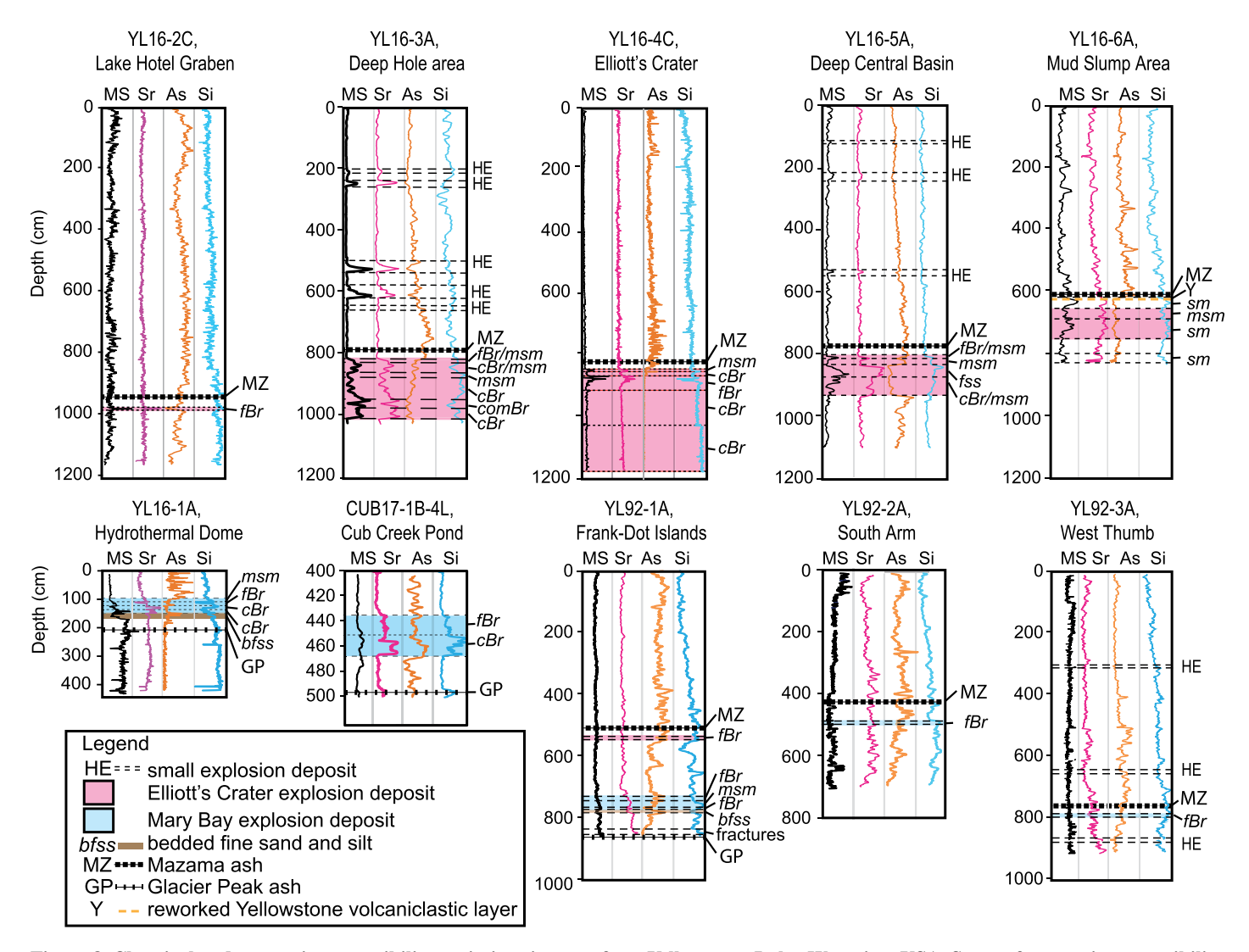


Figure 8. Chemical and magnetic susceptibility variations in cores from Yellowstone Lake, Wyoming, USA. Scans of magnetic susceptibility values (MS—black) and selected semiquantitative concentrations of key elements (Sr—magenta; As—orange; Si—blue) versus depth (cm). Note that depth in core CUB17-1B-4L, Cub Creek Pond, represents depth in drive -4L, not total depth. Abbreviations for hydrothermal explosion facies are the same as shown in the legend in Figure 4A and Table 2.

small hydrothermal explosion deposits. The deposits include fragments of silicified filamentous bacteria with inclusions of framboidal pyrite (Fig. 11G) and etched actinolite crystals having well-developed denticles (Figs. 11I and 11J).

Cores YL16-4A and YL16-4C: Elliott's Crater, a Compound Hydrothermal Explosion Crater

Cores YL16-4A and YL16-4C were collected adjacent to each other inside Elliott's Crater on the main crater floor (Figs. 1, 2, and 3D). Elliott's Crater is a large (0.4 km²) hydrothermal explosion crater with multiple smaller and younger explosion craters occurring within the main crater (Fig. 3D). A north-south seismic-reflection profile (A-A'; Fig. 3D) shows that the northern edge of the crater cuts into submerged shoreline terraces and lacustrine

deposits (Johnson et al., 2003). A 10-m-high crater rim of explosion debris on the northern edge drops steeply 40 m into the main flat crater floor where the cores were collected. Along the southern profile, still within the main crater, is a smaller (200 m wide), roughly circular, deeper (50–75 m) crater complex with active vents (Fig. 3D). Hydrothermal vent fluids were sampled at 57 m water depth from the smaller crater complex within the main crater and on the rim of the main crater at 11–12 m water depth (Gemery-Hill et al., 2007). South of Elliott's Crater, the elevation difference between the southern crater rim and the deep central lake basin floor is ~70 m.

Core YL16-4C provides a more complete sequence of hydrothermal explosion material from Elliott's Crater (Fig. 4A), but neither core penetrated the base of the explosion deposits. The Mazama ash occurs in cores YL16-4C and YL16-4A as a 5-mm-thick white layer ~22 cm above the top of the Elliott's Crater deposit at 8.20 m and 7.96 m depths, respectively.

The Elliott's Crater deposits are composed of thick (>3.3 m), continuous, normally graded hydrothermal explosion sequences that contain three hydrothermal explosion facies (*cBr, fBr, msm*) (Table 2). The hydrothermal explosion deposit is well sorted and contains sparse diatoms and abundant 30 to 50 µm grains of conchoidally fractured glass and quartz and broken crystals of feldspar (Fig. 10E) and actinolite. Many of the fragments have crystalline overgrowths, including aggregates of tiny quartz crystals (Figs. 11K and 11L) and a zeolite mineral, likely clinoptilolite (Fig. 11H).

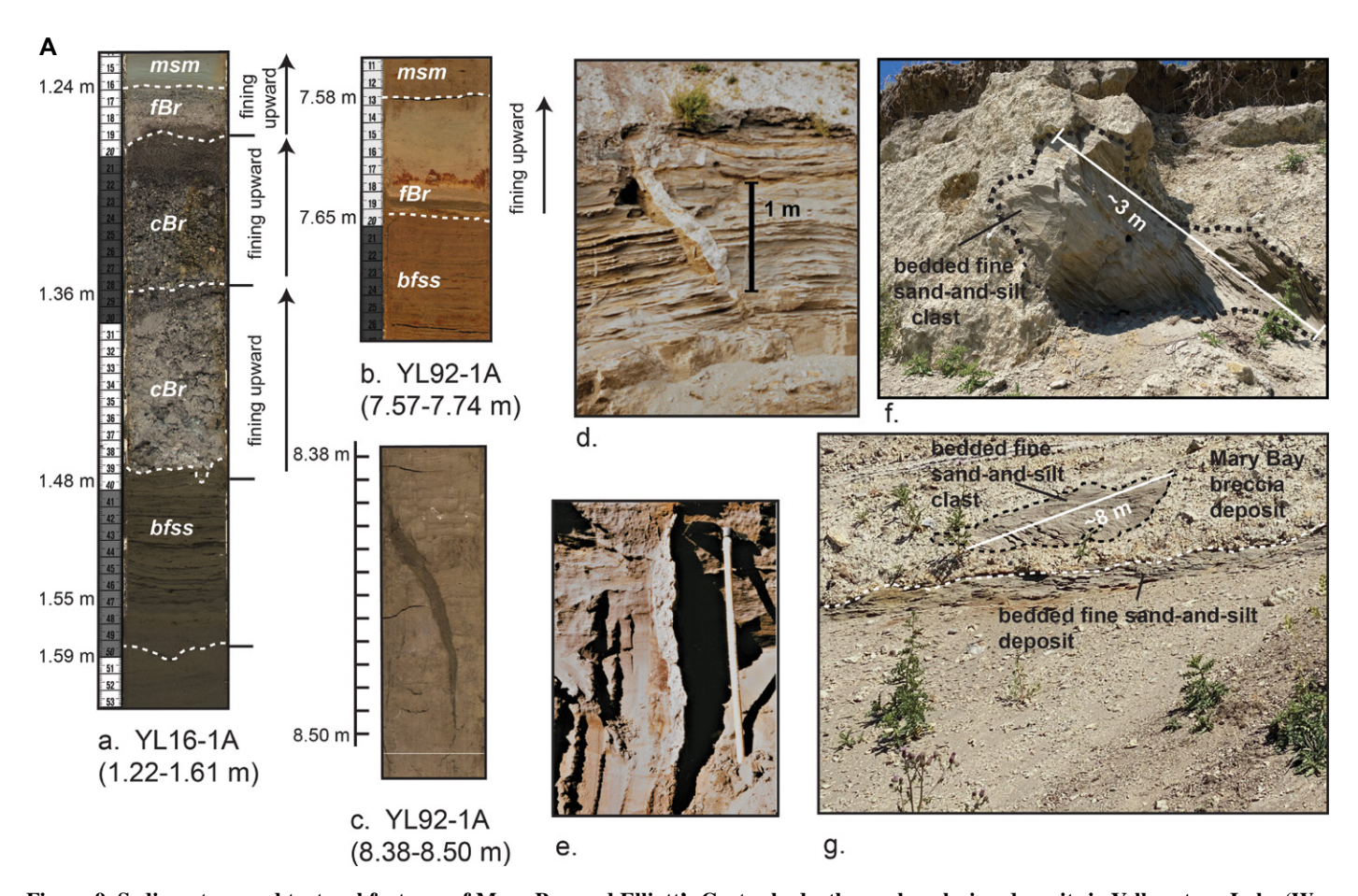


Figure 9. Sedimentary and textural features of Mary Bay and Elliott's Crater hydrothermal explosion deposits in Yellowstone Lake (Wyoming, USA) area and cores. Abbreviations are the same as used in Figures 4A (see legend), 4B, 7, and 8. Facies characteristics are detailed in Table 2. Locations of cores and their distances to Elliott's Crater and Mary Bay crater are detailed in Table S1. (A) Images showing textures of Mary Bay explosion deposits that are well sorted and fine upwards in piston cores in contrast to the poorly sorted Mary Bay explosion deposits exposed on land. (a) Multiple hydrothermal explosion facies with a well-sorted, clast-supported, coarse pebble deposit at base that fines upward. Below base of this unit is bedded fine-grained sand-and-silt deposit (bfss facies). (b) Well-sorted, fine-grained, distal primary fall hydrothermal explosion deposit (fBr facies) capped by suspension fallout deposit (msm facies). (c) 11-cm-long fracture filled with fine silt-sized hydrothermal explosion material in disturbed and faulted lacustrine sediment, interpreted as a high-pressure injection deposit into shallow soft lake sediments 13.7 km south-southwest of Mary Bay crater synchronous with the Mary Bay hydrothermal explosion. (d) Exposure in wave-cut terraces along northern shore of Yellowstone Lake of a large fracture filled with hydrothermal explosion breccia in faulted bedded sands. This proximal deposit is ~100 m west of the western margin of the Mary Bay explosion crater. (e) Exposure in wavecut terraces along northern shore of Yellowstone Lake of a large, >1-m-long fracture filled with Mary Bay hydrothermal explosion breccia in faulted, bedded sands. This exposure is ~150 m west of western margin of Mary Bay explosion crater. Garden tool (~1.0 m long) for scale. (f) Exposure in wave-cut terraces along northern shore of Yellowstone Lake of coarse, poorly sorted Mary Bay hydrothermal explosion breccia containing clasts with a large size range and diverse lithologic compositions. In the middle of the image is an ~3-m-long clast of bedded sand that was entrained in the explosion deposit. The sand clast is inferred to be from bedded tsunami sands exposed immediately below and in contact with the overlying Mary Bay explosion deposit. (g) Coarse, poorly sorted Mary Bay hydrothermal explosion breccia deposits with a large clast size range and a diverse lithologic composition, including the 8-m-long bedded sand and silt clast shown, is exposed as wave-cut terraces along the northern shore of Yellowstone Lake.

The lowest three meters of core YL16-4C (Fig. 4A) are composed dominantly of light gray to light medium-gray clay with an abundance (~10-15 vol%) of tiny (<2 mm), matrix-supported fragments, subangular to sub-rounded clasts, and flattened lenses of white clay (Fig. 9Be) and can be subdivided into various pulses of the explosion (Figs. 4A

and 8). Overall, the lowest three meters contain the greatest abundance of white clay clasts of various dimensions and clasts of black obsidian present either as single subangular fragments (<1–2 mm), discrete aggregates (up to 1 cm diameter), or layers of obsidian sand (Fig. 9Be). The lower 2.54 m of the explosion deposit contains a concentration of small

(2–4 mm) clasts of white chlorite-rich clay that increase in abundance and size (up to 5.8 cm by 1 cm) with depth (Fig. 7A). A white clay clast in gray sediment from 9.81 m depth (Fig. 10E) contains a 150 μm radial anhydrite crystal associated with quartz, feldspars, actinolite, clays (chlorite, smectite, illite), pyrite, and a few percent of diatoms, many of which are broken.

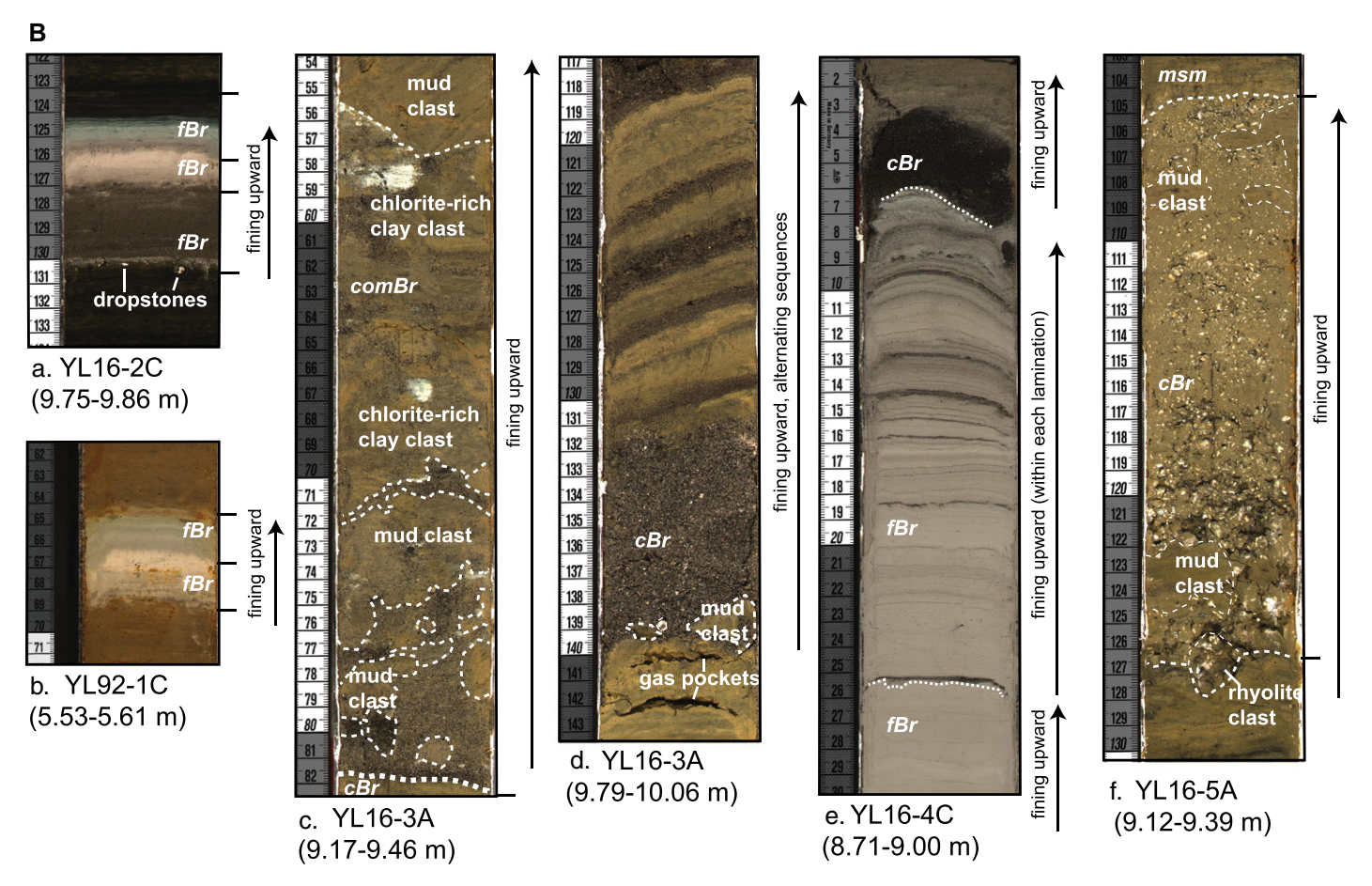


Figure 9. (Continued) (B) Images of Elliott's Crater hydrothermal explosion deposits within proximal and distal cores relative to Elliott's Crater. All deposits shown were emplaced in a subaqueous environment. (a) 7-cm-thick deposit comprising three units of fBr facies, each with a base containing small dropstones. (b) Fine-grained, fining-upward distal deposit. Note similarity in appearance to Elliott's Crater deposit in core YL16-2C within the Lake Hotel graben (Fig. 9Ba). (c) Facies comBr, containing abundant, variable mud clasts and white chlorite-rich clasts, is not as well sorted as most other Elliott's Crater deposits. (d) Facies cBr at base of deposit containing large dropstones of mud clasts and white, hydrothermally altered chlorite-rich clay in coarse black obsidian sand. This sequence grades upward into layers of coarse black obsidian sand alternating with layers of mud, representing multiple pulses in the explosion. (e) YL16-4C, 8.71-9.00 m depth: Multiple sequences of intracrater hydrothermal explosion deposits. The units in the upper explosion deposit generally are fine grained and reflect the highly altered nature of explosion debris. Layers of fine- to coarse-grained, black obsidian sand and silt layers alternate with hydrothermally altered gray clay, record multiple pulses in the waning stages of the explosion. (f) Facies cBr at base of deposit containing large dropstone clasts of white, hydrothermally altered rhyolite and mud.

Core YL16-5A: Floor of the Deep Central Basin

Core YL16-5A (Fig. 4A), collected 2.6 km south of Elliott's Crater on the nearly flat floor of the central lake basin at \sim 85 m depth (Figs. 1, 2, and 3D), contains seven limnic facies (Fig. 4A; Table S3) and four intervals of hydrothermal explosion deposits. The lowest of these deposits is the Elliott's Crater deposit (8.05 to 9.37 m depth), which is a thick (1.32 m) series of four sequences (Figs. 4A and 8). Collectively, each sequence fines upward with the lowest sequence being coarsest (facies cBr) with the lowermost containing a 2.8-cm-diameter clast of altered rhyolite as a dropstone at its base (Figs. 7A and 9Bf). In the interval from 8.48 to 8.58 m depth,

facies *msm* caps facies *fss* (Table 2) and contains light tan, wispy or feathery textures and minor amounts of small (1–2 mm thick, <5 mm long) white clastic fragments (Fig. 7B). SEM and XRD analyses (Fig. 10F) at 8.53 m depth show altered and encrusted clumps of diatom fragments with clasts of volcanic glass, anhydrite, feldspars, quartz, and clays (chlorite, smectite, minor illite).

At 7.79 m depth, the Mazama ash is a thin, 5-mm-thick layer occurring 24 cm above the top of the Elliott's Crater deposit. Above the Mazama ash, three thinner (1 to 7 cm thick), less complex, normally graded, hydrothermal explosion deposits (1.16–1.17 m, 2.10–2.37 m, 5.31–5.38 m depths, Figs. 4A and 8). Each sequence has a composition rich in broken frag-

ments of feldspar crystals and conchoidally fractured quartz and obsidian, and rare actinolite grains.

Core YL16-6A: Steep Eastern Shore of Yellowstone Lake

Core YL16-6A (Fig. 4A) collected along the eastern shoreline of Yellowstone Lake sampled the toe of a slump (Fig. 1; Table S1; Johnson et al., 2003). Bathymetric and seismic-reflection data (Figs. 1, 2, and 3E) show a hummocky topography with scalloped edges and chaotic seismic reflectors at >6 m depth. The geochemical patterns are subdued in the lower 2+ m of the core compared to those of undisturbed hydrothermal explosion deposits in other cores (Fig. 8).

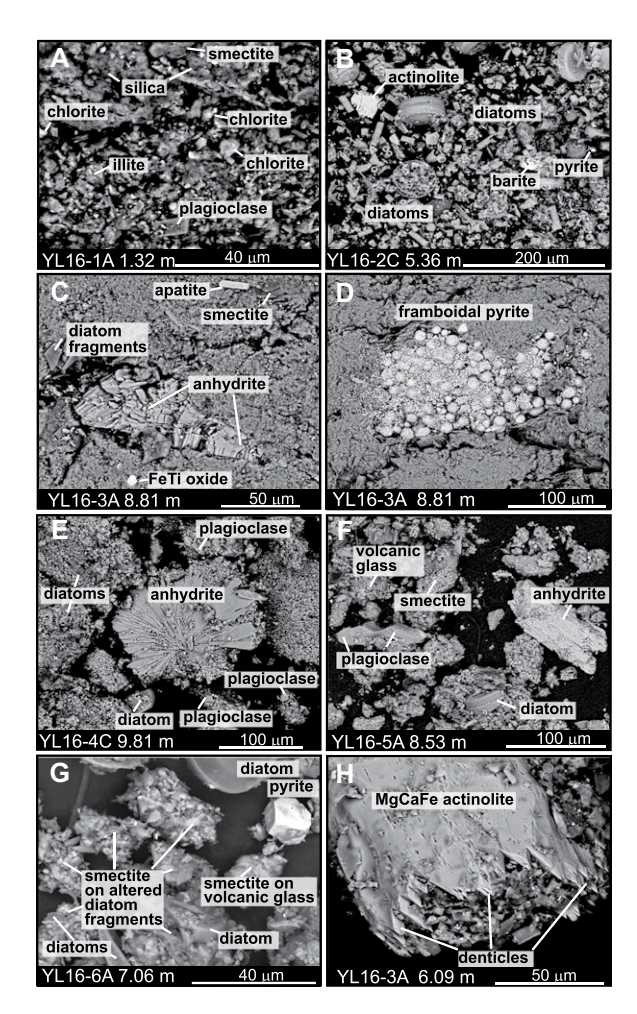


Figure 10. Scanning electron microscope (SEM) backscattered electron images of hydrothermal explosion deposits in sediment cores from Yellowstone Lake, Wvoming, USA. Minerals were identified using textural information and spot analyses for chemical constituents; additionally, mineralogy was confirmed using X-ray diffractometry (XRD) on bulk samples and clay separates. (A) Facies cBr of Mary Bay explosion deposit. SEM image shows strongly silicified and clayencrusted grains (smectite, chlorite, and illite). Pyrite, anhydrite, fractured quartz, feldspar, and actinolite also are present. (B) Detrital, diatom-rich unaltered sediment. Sample is ~4.4 m above top of Elliott's Crater hydrothermal explosion deposit and contains mostly diatoms and diatom fragments with some rhyolitic glass clasts, an actinolite grain with denticles, and feldspar clasts (not shown). Sparse barite and pyrite are present. (C) Facies cBr of Elliott's Crater explosion. Sam-

ple is from 1-cm-by-3-cm clast of white angular chlorite-rich clay with fine-grained silicified matrix and large (150 µm) anhydrite crystal aggregate. Also present are local diatom fragments, framboidal pyrite (see 10D), smectite, chlorite, illite, Na-Ca feldspar, apatite, Fe-Ti oxide, sphene, and quartz. (D) (same depth as 10C) Framboidal pyrite masses ~150 µm long, with 1 µm cubes and 10 µm spherical masses. Framboids generally are considered to represent bacterial production of sulfide during diagenesis (Goldhaber, 2003); sulfur isotope data from the Deep Hole vent area support this assertion (Fowler et al., 2019b). (E) Facies cBr of Elliott's Crater deposit. Sample has matrix of massive, light-gray, clay-rich sediment containing ~20% white clay clasts (generally <0.5 cm and flattened) with subordinate black obsidian silt. SEM image shows 150 µm wide radial anhydrite crystal from white chlorite-rich clay clast, Na-Ca feldspars, matrix of fine-grained (generally <10 µm) fragments cemented by silica and with abundant clay alteration to chlorite and smectite, pyrite cubes and framboids (not shown in this photo), and small percentage of diatoms and diatom fragments. (F) Facies fss from Elliott's Crater explosion deposit with deformed elongated white mud clasts. SEM image shows minor diatoms and altered and encrusted clumps of diatom fragments, abundant volcanic glass clasts, and plagioclase and K-feldspar clasts. Also present is 125-um long anhydrite crystal, abundant altered smectite, Mg-Fe chlorite, quartz, Feoxides, and ilmenite. (G) White-tan elongate 1-cm-by-6-cm clay clasts in facies sm that incorporated the Elliott's Crater hydrothermal explosion deposit. SEM image shows subrounded glass grains altered to smectite, clusters of minerals and diatom fragments, diatoms strongly altered to smectite, and a 20-um pyrite cube. (H) Fine-grained sand layer at top of smaller, probably locally sourced, hydrothermal explosion deposit shows large (~300 μm) actinolite crystal with distinctive, jagged denticles on one end. Denticles likely formed during hydrothermal alteration (Phillips-Lander et al., 2014).

Deposits in the lower 2 m of the core contain multiple sulfidic muds (facies *sm*), with an overall streaky or mottled texture, and thin lenses of black obsidian sand (Fig. 7C). Some of the units within this interval have steep dips, due to disturbance during mass movement. We interpret the units as mud slump deposits where blocks of mud moved downslope a short distance.

The basal slump package (6.27-8.41 m, Fig. 4A) was subdivided into three sequences that reflect different episodes of mass movement; all involved the incorporation of hydrothermal explosion debris (either from Elliott's Crater or elsewhere) as indicated by the relative enrichment of Sr, depletion of As, and high values of magnetic susceptibility, compared to lake sediment (Figs. 4A and 8). The sequence between 7.03 and 7.61 m depth contains abundant clasts of angular to rounded, white chlorite-rich clay. A 1 cm by 6 cm clay clast from 7.06 m depth (Fig. 10G) shows fresh diatoms, clusters of diatom fragments strongly altered to smectite, subrounded volcanic glass with smectite alteration on surfaces, pyrite crystals, and local anhydrite (not shown in Fig. 10G). The uppermost sequence (6.21 to 6.66 m depth) contains reworked Yellowstone volcaniclastic ash dipping ~25° near its top (Fig. 4A; Table S2). At 6.18 m depth, a 5-mm-thick layer of Mazama ash is present and appears less planar and more irregular than in other Yellowstone Lake cores. Bedding in the core is generally planar above the Mazama ash.

The 1992 Yellowstone Lake Sediment Cores and 2017 Cub Creek Pond Sediment Cores

Cores YL92-1A and YL92-1C between Frank and Dot Islands

Cores YL92-1A and YL92-1C, collected in 1992 from adjacent locations, are between Dot Island and Frank Island (Fig. 1). The longer core, YL92-1A, has the more complete geologic record and contains eight limnic facies, two ash layers, and two hydrothermal explosion deposits interbedded with the lacustrine sediments (Tiller, 1995) (Figs. 4B and 8).

Near the base of core YL92-1A (Fig. 4B), Glacier Peak ash, a 1- to 2-mm-thick white tephra, occurs at 8.54 m depth (Tiller, 1995; this study) and contains small (~2 mm) displacements. Above the Glacier Peak ash, two irregularly shaped, sand-filled fractures crosscut a 20-cm-thick zone of faulted lacustrine sediments (Fig. 9Ac). The fractures are at depths between 8.32 and 8.50 m, 4 cm above the Glacier Peak ash, and are located 42 cm beneath the base of bedded sand-and-silt deposits (facies *bfss*) that underlie the Mary Bay explosion deposit (Figs. 4B and 8). SEM examination of a sample from the

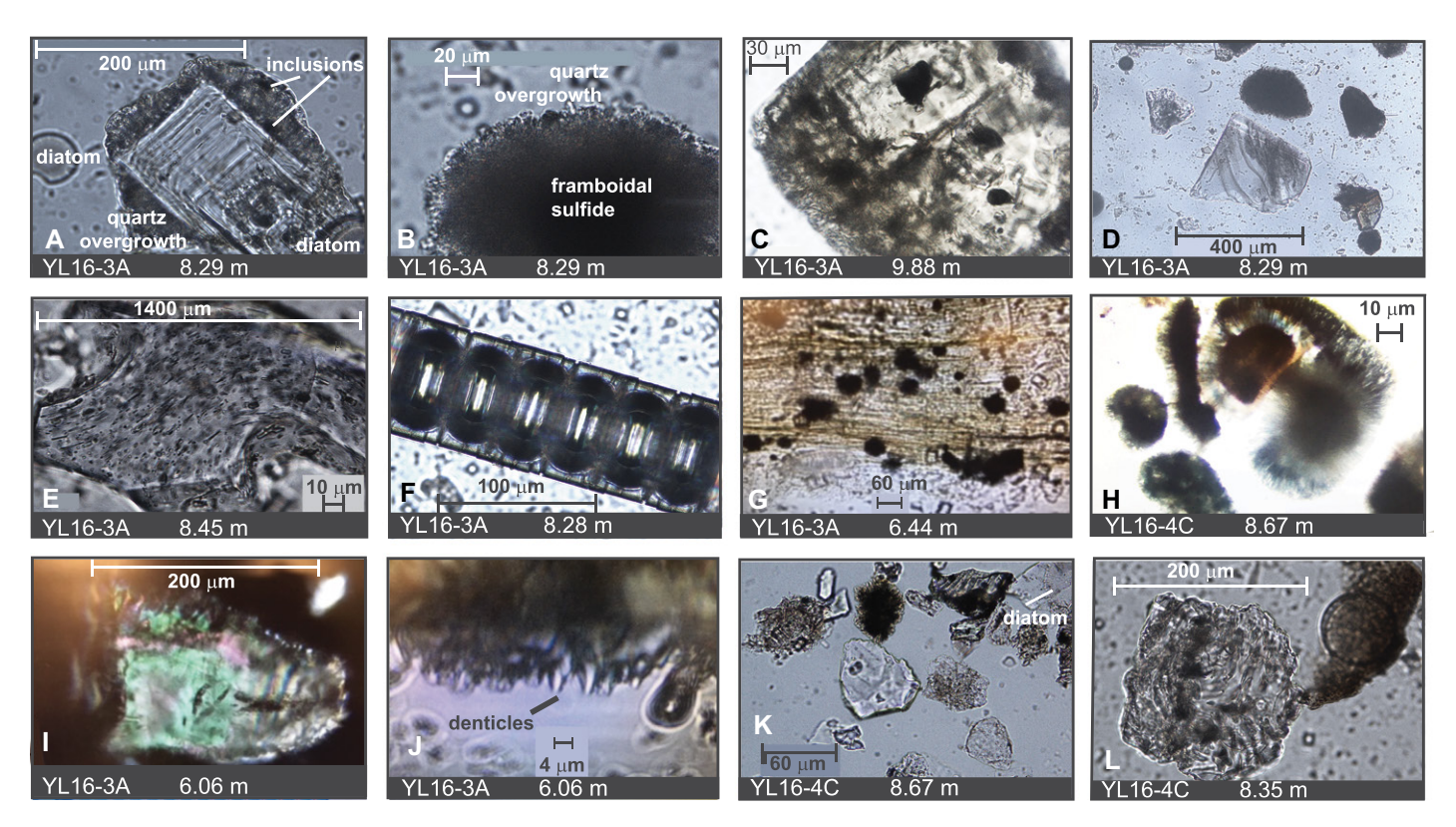


Figure 11. Petrographic images of samples from hydrothermal explosion deposits in Yellowstone Lake (Wyoming, USA). (A) Elliott's Crater hydrothermal explosion deposit. Zoned feldspar crystal with overgrowth of secondary hydrothermal quartz; note opaque, likely pyrite, inclusions within quartz. (B) Elliott's Crater hydrothermal explosion deposit. Mass of opaque crystals (framboidal pyrite) with overgrowth of euhedral quartz. (C) Image of a large (~200 μm) hydrothermal quartz crystal with small (~30 μm), rounded and opaque (framboidal pyrite, obsidian?) inclusions. Sample from 2-cm-thick layer of black sand in Elliott's Crater hydrothermal explosion deposit. (D) Variety of clasts collected from pocket of dark sand from Elliott's Crater explosion deposit. The 400-µm-wide angular fragment in center is a flow-banded rhyolitic glass; note conchoidally fragmented edges. (E) Clast of flow-banded rhyolitic glass found in pocket of dark sand from facies cBr in Elliott's Crater explosion deposit. (F) Long segmented Stephanodiscus yellowstonensis diatom collected near base of facies fBr from Elliott's Crater hydrothermal explosion deposit. (G) Silicified filamentous bacteria containing small (10–60 µm), opaque grains of framboidal pyrite, Small fragments in background are tiny (1–5 μm) diatoms. This sample is from a small local hydrothermal explosion deposit at 6.41–6.48 m depth. (H) Obsidian grains overgrown by rosette-like blades of zeolite, probably clinoptilolite (Bargar and Beeson, 1981). Sample collected from ~1 cm round pocket of predominantly obsidian grains in facies fBr of Elliott's Crater hydrothermal explosion deposit. (I) Broken and etched actinolite crystal with tiny surficial denticles from a small hydrothermal explosion deposit from 5.75 to 6.10 m depth. (J) Magnified image of tiny (<4 microns) denticles from Figures 11I and 10H. (K) Diverse clasts from near base of facies fBr in Elliott's Crater explosion deposit. Most fragments are hydrothermal botryoidal quartz with opaque inclusions. The dark fragment at top is a cluster of framboidal pyrite with overgrowths of hydrothermal, bipyramidal quartz. Clear fragment below dark fragment is a tephra shard with chattered edges. Large (~50 µm), unbroken diatom in upper right corner most likely was in water column and rained down with the deposit, not being part of original explosion debris. (L) Hydrothermal quartz crystal with opaque inclusions. Note conchoidally fractured edges of quartz crystal. Darker fragment on right is hydrothermal botryoidal quartz with tiny opaque inclusions. Sample from msm facies, capping Elliott's Crater hydrothermal explosion event.

upper fracture indicates that the material is hydrothermally altered and rich in obsidian, clay, and sinter grains, and has similar chemical and physical characteristics to explosion deposits observed in other sediment cores. The clasts are mostly of 10– $60~\mu m$ diameter, subrounded to angular, rhyolitic glass grains with surface alteration of the glass by silica, smectite, and chlorite, plus minor grains of actinolite. Sediments in both fractures have high values of magnetic susceptibility and are enriched in Sr relative to the lacustrine sediments (Fig. 8).

At 7.65 to 7.79 m depth (Fig. 4B), a 14-cm-thick, finely bedded, normally graded, fine sand-and-silt unit (facies *bfss*) grades upward to the base of the Mary Bay hydrothermal explosion deposit. Above this, the lower Mary Bay explosion deposit occurs as a 7-cm-thick sedimentary sequence (7.58 to 7.65 m depth, facies *fBr*) that fines upwards from a fine sand to a light bluish-gray clay (Figs. 9A) and is capped by 20 cm of suspension fallout mud (facies *msm*). An upper 1-cm-thick Mary Bay deposit (7.37–7.38 m depth) fines upwards

from a fine silt to a light gray clay capped by a 1-mm-thick light tan clay (Fig. 4B).

Continuing upward in core YL92-1A is the 3-cm-thick, normally graded Elliott's Crater hydrothermal explosion deposit at 5.32 to 5.35 m depth. The base of this unit is slightly irregular; a 7-mm-thick, fine-grained siltstone at the base grades upward to a pale bluish-gray clay. At 5.07 m depth, a second tephra is the 5-mm-thick Mazama ash.

The adjacent core YL92-1C (Fig. 4B), previously unopened, also is described and sampled

in the present study. The Mary Bay explosion deposit occurs near the base of the core as a normally graded silt capped by two fBr facies separated by \sim 7 cm of facies msm. Farther up in the core is a 5-cm-thick section of the Elliott's Crater explosion deposit (5.54 to 5.59 m depth). At 5.25 m depth is the 5-mm-thick Mazama ash. The Elliott's Crater explosion deposit in this core is similar in appearance to the equivalent unit in core YL16-2C from the Lake Hotel graben (Fig. 9Bb) despite being about twice as distant from the source crater (11.9 km vs 5.2 km).

Core YL92-2A: South Arm

Core YL92-2A (Fig. 4B) is 6.87 m long and was collected at 52 m depth on the flank of a sublacustrine sedimentary ridge at the mouth of the South Arm (Figs. 1 and 4B; Tiller, 1995). The Elliott's Crater explosion deposit occurs as a ~2-cm-thick, normally graded sequence (4.93 to 4.95 m depth) and contains 1–4 mm, rounded, gray clay clasts at its base that are in the underlying lacustrine sediment. At 4.26 m depth, the 5-mm-thick Mazama ash is 67 cm above the Elliott's Crater deposit, representing a greater depth interval between the Mazama and Elliott's Crater deposit than in other cores.

Core YL92-3A: West Thumb

Core YL92-3A (Fig. 4B), collected in the northwest West Thumb basin, is located north of a hydrothermal dome in an area with abundant small hydrothermal domes and gas pockets (Fig. 1; Morgan et al., 2007b). The core contains several fining-upward sequences with

hydrothermal signatures. A 1-cm-thick, finingupward sequence occurs at 8.80-8.81 m depth. Above this at 7.91 to 7.93 m depth, the Elliott's Crater explosion deposit occurs as a 2-cmthick, fining-upward sedimentary sequence. The unit overall is mostly composed of altered clay but contains subtle, upward-fining changes in grain size and color. The Elliott's Crater deposit, capped by a 1 mm white clay, has an uneven upper contact. The 5-mm-thick Mazama ash is at 7.60 m depth below two additional 1-cm-thick, fining-upward sequences at depths of 6.47-6.48 m and 3.01-3.02 m. Both consist of fine-grained clay layers with tiny fragments below their planar bases. We interpret all four fining-upward deposits in core YL92-3A as hydrothermal explosion deposits (Figs. 4B and 8).

The 2017 Cub Creek Pond Sediment Cores

Core CUB17-1B (Figs. 1 and 4B) contains the Glacier Peak ash as a 2-cm-thick white tephra at 4.95 to 4.97 m depth. The ash layer dips $\sim 14^{\circ}$, has a non-planar base, appears disturbed, and is considerably thicker than occurrences observed in sediment cores within Yellowstone Lake, which may relate to reworking of ash in a small water body (0.014 km²; Lu et al., 2017; Schiller et al., 2020). Above the Glacier Peak ash is the Mary Bay hydrothermal explosion deposit (4.34 to 4.65 m depth), a 31-cm-thick complex series of normally graded, hydrothermally altered sediments divided into four sequences based on lithologic, chemical, and physical characteristics (Figs. 4B and 8). Arsenic is not depleted relative to the coarse sediment detritus in the pond.

Gravity Cores

Among the 27 gravity cores collected between 2016 and 2018, three contain thin, normally graded sequences with strong hydrothermal signatures (Fig. 12). Two cores are from the Deep Hole vents and one is from the Bridge Bay area (Figs. 1 and 3C). All are short cores (<1 m in length) and none contain tephra. The hydrothermal explosion deposits in the short cores are important in establishing very young explosion activity.

DISCUSSION

Dynamic Geologic Processes and Sedimentation Rates in Yellowstone Lake

Previous multibeam bathymetric mapping and seismic-reflection profiling have revealed that complex geologic processes are ongoing in the dynamic Yellowstone Lake basin (Johnson et al., 2003; Morgan et al., 2007a, 2007b). Hydrothermal explosion deposits are present in 17 of the 18 cores examined in this study. Many are previously unidentified, confined to the lake basin, and provide important insight into active geologic processes. Average sedimentation rates for the northern part of the lake (1.06 m/k.y.) and West Thumb basin (1.04 m/k.y.) indicate a generally steady history of sediment accumulation, and deviations from normal sedimentation rates provide constraints on the timing of faulting events and other processes. For example, a much lower apparent

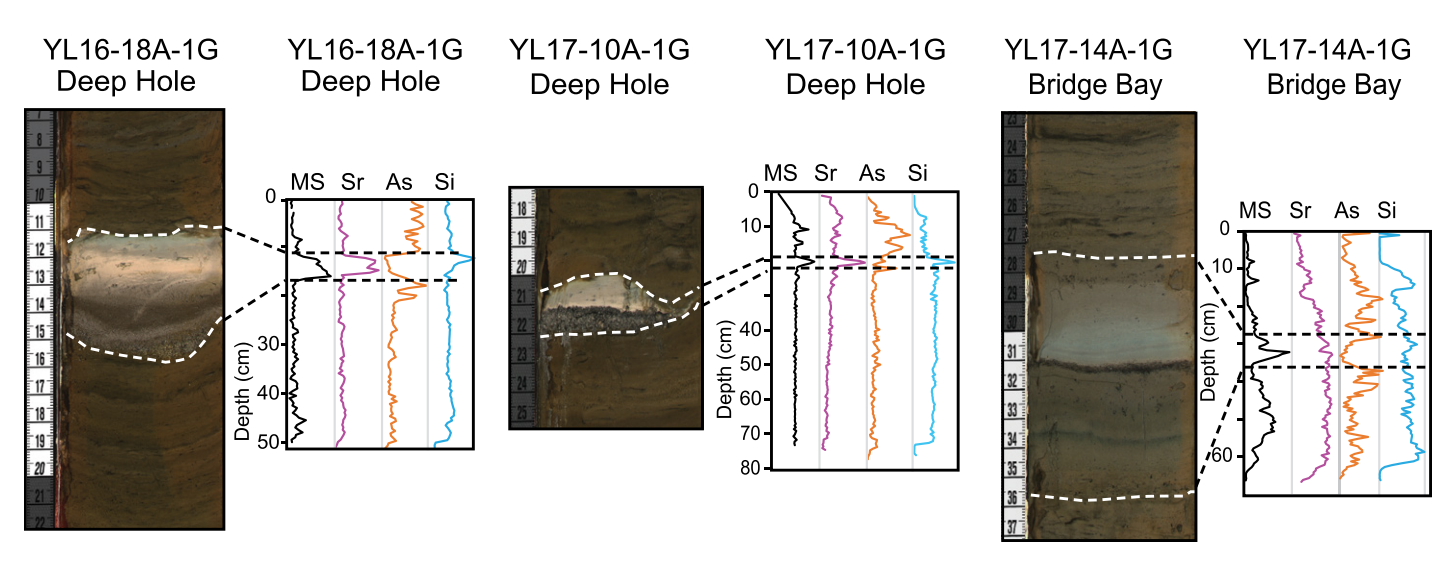


Figure 12. Gravity cores YL16-18A-1G and YL17-10A-1G (from the Deep Hole area) and YL17-14A-1G (from the Bridge Bay area) showing thin (2 to 5 cm thick), fining-upward sedimentary sequences in cores from Yellowstone Lake, Wyoming, USA. The deposits are at depths of 11–36 cm and are interpreted to derive from small hydrothermal explosions that formed roughly 160–360 years ago (1860–1660 CE), based on rates of sedimentation in the northern lake, and are probably of local origin. Scans show higher values of magnetic susceptibility (MS), As depletion, and Sr and Si enrichment for the hydrothermal explosion deposits, relative to lacustrine deposits. Si concentrations are enriched in the finer portions of these deposits relative to normal lake sediments.

rate of 0.15 m/k.y. calculated for YL16-1A (Fig. 5) is attributed to uplift at a rate of 0.94 m/k.y. that caused shedding of overlying sediments from the over-steepened dome. Likewise, the sedimentation rate within the Lake Hotel graben appears to be ~ 1.20 m/k.y., a higher rate than is typical for the northern lake, likely due to sloughing of material into the active graben. In contrast, along the steep eastern shore of the lake, the depth of the Mazama ash in core YL16-6A is shallower than in most of the northern lake suggesting an apparent sedimentation rate of 0.82 m/k.y.; this likely is due to removal of overlying units. The lower sedimentation rate determined for the southern part of the lake (0.62 m/k.y., Fig. 5) is considered accurate and due to isolation from the main body and deeper basin of the lake (Tiller, 1995).

Seismic Activity and Faulting in Yellowstone Lake

Seismic activity and faulting are important controls on hydrothermal activity. Three sets of active extensional features are recognized in Yellowstone Lake (Morgan et al., 2007a, 2007b; Bouligand et al., 2020; Fig. 1): (1) the 25-kmlong Eagle Bay fault zone that extends from the southern lake northward and includes the Lake Hotel graben and a fault near the Yellowstone River farther north (Figs. 1 and 13A; Christiansen, 2001; Johnson et al., 2003; Locke et al., 1992; Pierce et al., 2007); (2) the northwest-trending set of fractures and faults east of Stevenson Island (Cash, 2015; Johnson et al., 2003; Figs. 1 and 3C); and (3) the northeast-trending set of parallel fractures including the active Weasel Creek-Storm Point lineament and the active Elephant Back fissure system (Morgan et al., 2007a, 2009; Fig. 1). The Elephant Back fissures extend northeast between the Mallard Lake and Sour Creek resurgent domes (Christiansen, 2001) and are related to active deformation of the Yellowstone Caldera (Dzurisin et al., 1990, 1994, 2012; Wicks et al., 2006). Long-term (~15 k.y.) changes in postglacial lake level, as indicated by shoreline terrace elevations along the northern lakeshore and north into the Yellowstone River valley, are a product of two processes: inflation-deflation cycles due to active deformation of the Yellowstone Caldera and erosion of the lake outlet in the Yellowstone River north of Fishing Bridge (Dzurisin et al., 2012; Locke and Meyer, 1994; Meyer and Locke, 1986; Pierce et al., 2007).

Farther south, the Eagle Bay fault zone, which has been active at least for the past 13 ka, is a discontinuous set of fault segments that splays west-to-east across a \sim 3-km-wide band along the western edge of the main Yellowstone Lake basin (Fig. 1). A seismic-reflection profile from

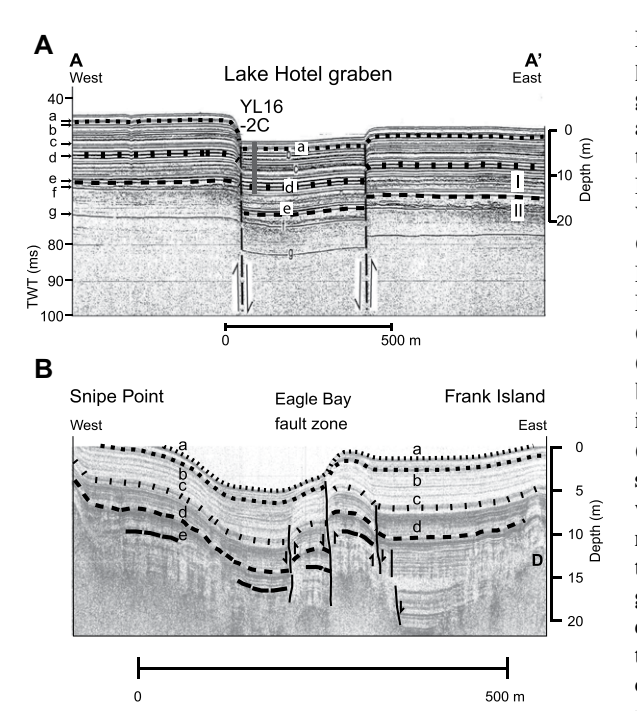


Figure 13. Seismic-reflection profiles from the Lake Hotel graben (Johnson et al., 2003) and from 1992 coring operations between Snipe Point and Frank Island, Yellowstone Lake, Wyoming, USA (Fig. 1) (from Continental Scientific Drilling Facility archive at University of Minnesota, Twin Cities, USA). (A) Seismic-reflection profile (Fig. 3C) of the Lake Hotel graben (Johnson et al., 2003) showing location of core YL16-2C (black vertical line). Assuming a sedimentation rate of 1.2 m/k.v. within the graben and a sedimentation rate of 1.06 m/k.y. in the northern lake outside the graben, reflector "d" represents deposition at ca. 8 ka and reflector "e" represents deposition at ca. 13 ka. (B) Seismic-reflection profile of Snipe Point to Frank

Island. Assuming an average sedimentation rate of 0.62 m/k.y. based on data from the southern lake (Fig. 5), line "b" (at ~1 m depth) represents deposition ~1500 years ago, line "c" (average depth 5 m) represents the timing of the Elliott's Crater explosion event at ca. 8 ka, line "d" represents the timing of the Mary Bay explosion event at ca. 13 ka (average depth 8.5 m), and line "e" represents a non-continuous reflector, which corresponds to ~15 k.y. The most recently active fault has ~1 m displacement and occurred ~1500 years ago; faulting resulted in 2.8 m of displacement at ca. 8 ka (offset of line "c"), and ~0.7 m of displacement at ca. 13 ka (offset of line "d"). D represents an area of hydrothermal doming that appears to have ceased activity by ca. 8 ka. No offset is present in surficial sediments, indicating displacement has not occurred on this fault since ~1500 years ago. TWT—two-way travel time.

Snipe Point to Frank Island (Figs. 1 and 13B) shows a record of repeated faulting with significant displacements up to several meters extending into sediments of early postglacial age. We estimate that fault displacement events occurred at ca. 8 ka resulting in a net offset of \sim 2.8 m and at ca. 13 ka resulting in a net displacement of \sim 0.7 m (Fig. 13B). The most recent displacement of \sim 1 m in the profile occurred \sim 1500 years ago (Fig. 13B).

The Role of Water in Hydrothermal Explosions in Yellowstone Lake

The hydrostatic pressure exerted on hydrothermal systems at lake-floor vent sites is governed by water depth that dramatically affects boiling temperatures of hydrothermal vent fluids (Balistrieri et al., 2007). Studies of lake shoreline terraces (Pierce et al., 2007) suggest water depths would have been ~5 m deeper (S2 shoreline) than present before the 8 ka Elliott's Crater explosion and ~17 m deeper than present at 13.6 ka (S5.5 shoreline) prior to the Mary Bay explosion. The

depth-dependent hydrostatic load of the lake limits phase separation by maintaining higher pressure and temperature conditions at sublacustrine hydrothermal vents (12 atm, 174 °C in the Deep Hole vent field; 5.3 atm, 141 °C in the Southeast-West Thumb (SE-WT) vent field (Fowler et al., 2019c). In contrast, subaerial hot springs are limited by the surficial boiling temperature of 92 °C at the altitude of the Yellowstone Plateau.

Variations in Cl concentrations in vent fluids from different areas within the lake show that some ascending fluids are acidic, low-Cl (vapordominated) fluids (Figs. 3A and 3C) whereas others are liquid-dominated alkaline-Cl fluids (Figs. 3D and 3F). Like the subaerial systems, ascending deep-seated alkaline-Cl hydrothermal fluids beneath the lake experience decompressional boiling wherein liquids reach pressure-temperature conditions corresponding to the boiling point of water. Phase-separated steam with non-condensable dissolved gases, mainly CO₂ and H₂S, generate vapor-dominated fluids that produce low-Cl sublacustrine vent fluids, as exemplified in the Deep Hole vent field (Figs. 1

and 3C). Following boiling, the residual subsurface hydrothermal fluids become progressively enriched in Cl to \sim 9–22.5 mmol/L due to boiling/steam loss, which also produces more alkaline pH values due to loss of CO₂ and hydrolysis reactions with silicates. Overall, evolution of the deep-seated alkaline-Cl fluid generally involves boiling, mixing with meteoric waters, and conductive cooling, which either increases or decreases the Cl content of the fluids depending on the pathway (Balistrieri et al., 2007; Fournier, 1989; Fowler et al., 2019c; Hurwitz and Lowenstern, 2014; Rye and Truesdell, 2007; Shanks et al., 2005; Truesdell et al., 1977).

The composition of active hydrothermal vent fluids in the post-explosion craters provides evidence of the fluids that created the Mary Bay and Elliott's Crater hydrothermal explosions. Mary Bay and Elliott's Crater vent fluids (Figs. 3D and 3F) are mostly alkaline-Cl but a few vents are low Cl compared to normal lake water (140 \pm 20 μmol/L) (Balistrieri et al., 2007; Gemery-Hill et al., 2007). The strongest evidence for the dominant role of alkaline-Cl fluids at Mary Bay comes from high Cl values (7.6 mmol/L) in shallow pore water of a hot core taken from a deep vent area (Fig. 3F) and samples containing higher than normal Cl (175-197 µmol/L) in the Mary Bay water column above the vents (Aguilar et al., 2002; Balistrieri et al., 2007). Both alkaline-Cl and low-Cl vent fluids have been sampled at Elliott's Crater on the southern crater rim (Fig. 3D) and pore water studies of core YL16-4C from the crater floor show high-Cl pore fluids at depth (Gemery-Hill et al., 2007; Shanks et al., 2019). The predominance of alkaline-Cl hydrothermal vent fluids suggests that both the Mary Bay and Elliott's Crater explosions resulted from alkaline-Cl liquids that flashed to steam.

Mineralogy of the Hydrothermal Explosion Deposits

The fundamental mineralogy and mineral chemistry of the hydrothermal explosion deposits in Yellowstone Lake cores provide further evidence of the hydrothermal processes and types of fluids that altered the host sediments and rocks prior to explosion. Sediments largely unaffected by hydrothermal alteration (Fig. 10B, core YL16-2C) contain abundant whole and broken diatom frustules with minor amounts of detrital and broken grains of rhyolitic glass, feldspars, quartz, and occasional actinolite grains.

Samples of the Mary Bay and Elliott's Crater hydrothermal explosion deposits in the sediment cores (Figs. 10 and 11) show the effects of alteration within pre-explosion, sublacustrine hydrothermal systems that produced abundant smectite, chlorite, and fine-grained quartz or silica that

coat and cement grains. Other common alteration phases include illite, quartz, albitic plagioclase, actinolite, pyrite, and anhydrite (Fig. 10).

Actinolite crystals in the explosion deposits have ragged, 5–30 μm denticle textures (Figs. 10H, 11I, and 11J). Phillips-Lander et al. (2014) showed that fresh amphibole placed in subaerial acid-sulfate hot springs (T = 43–90 °C, pH = 2.4–5.8) for 6–24 h is dissolved along cleavage planes, producing textures analogous to denticles. Although denticular amphiboles have been found in surficially weathered zones (Velbel, 2007), the actinolite in Yellowstone Lake sediments likely is hydrothermal. Actinolite is a typical alteration phase in active continental hydrothermal systems at temperatures >280 °C (Bird et al., 1984; Chambefort et al., 2017).

Elongate, conspicuous, angular clasts composed of white, chlorite-rich clay (typical dimensions 0.5–1 cm by 3–6 cm) are prominent in the lower 2.5 m of the proximal primary fall hydrothermal explosion deposits (facies *cBr*) from Elliott's Crater. SEM and XRD studies (Figs. 10C, 10E, 10F, and 10G) indicate that the samples are fine-grained and contain small diatom and mineral fragments (<5 um) with abundant chlorite and smectite alteration. All samples

contain blocky, Na- and K-rich feldspar grains, some quartz, and the typical accessory minerals of pyrite, iron-titanium oxides, illite, and apatite.

A common feature of the white chlorite-rich clay clasts is the occurrence of large ($150 \mu m$) anhydrite crystals (Fig. 10C, 10E, and 10F). The occurrence of large anhydrite crystals in the white clay clasts indicates that anhydrite was stable in the pre-explosive alteration system. Anhydrite and gypsum also are common hydrothermal minerals in vent muds from Mary Bay and the Deep Hole vent field, reflecting CaSO₄ precipitation in shallow but high-temperature, near-vent portions of the hydrothermal system (Shanks et al., 2005, 2007).

Phase Relations

Hydrothermal mineralogy of the hydrothermal explosion deposits from both Mary Bay and Elliott's Crater is consistent with an origin in large, well-established hydrothermal vent fields in the sublacustrine environment. Equilibrium phase relations among representative alteration minerals are shown on a T(°C)-log aSiO₂ diagram (Fig. 14). The fluid composition used to construct this diagram approximates that of

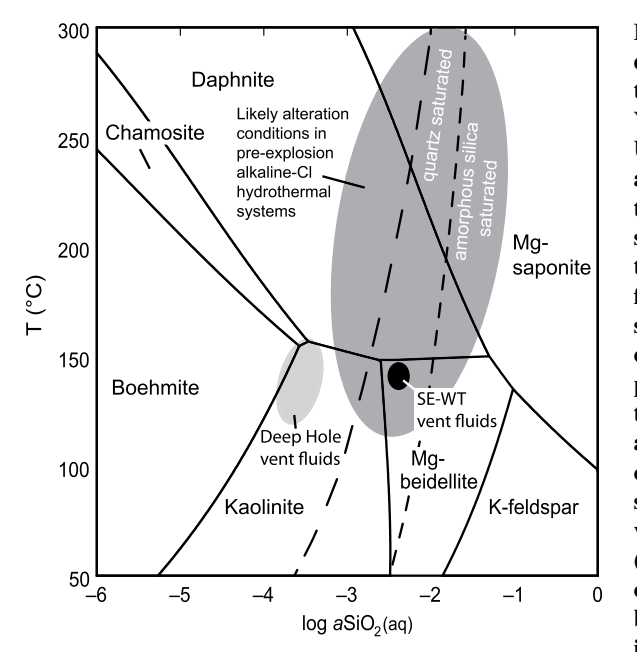


Figure 14. Mineral stability diagram plotting temperature (°C) vs. log aSiO₂(aq) for Yellowstone Lake (Wyoming, USA) hydrothermal systems hydrothermal alteration in pre-explosion thermal systems. This diagram shows that boehmite, kaolinite, Kfeldspar, smectites (beidellite, saponite), and chlorites (chamosite, daphnite) are stable phases in Yellowstone hydrothermal systems. Quartz and amorphous silica saturation curves are shown for comparison. Data for Yellowstone Lake vent fluids from Fowler et al. (2019a, 2019c) are shown for comparison, and mineral stabilities agree with those found in near-vent alteration at Deep

Hole (kaolinite, boehmite) and Southeast-West Thumb (SE-WT) field vents (beidellite, quartz). Diagram uses log activity values of species, as follows: pH = 4.7, HCO $_3^-$ = -1.87, SO $_4^-$ = -3.063, Cl $^-$ = -3.824, Na $^+$ = -2.824, K $^+$ = -3.699, Mg 2 + = -3.222, Ca 2 + = -3.229, Fe 2 + = -3.523. Values are intermediate between those of neutral to alkaline-Cl SE-WT field vent fluids and vapor-dominated Deep Hole fluids of Fowler et al. (2019a, 2019c). Reactions in pre-explosion hydrothermal systems at Mary Bay and Elliott's Crater likely took place at temperatures of 100–300 °C with SiO $_2$ (aq) near saturation with quartz and amorphous silica. Alteration phases stable at these conditions include smectites (beidellite and saponite), chlorites (daphnite and chamosite), quartz, and amorphous silica as observed in alteration assemblages in hydrothermal explosion deposits (Fig. 10).

hotter vent fluids in the vapor-dominated Deep Hole and SE-WT alkaline-Cl vent fields (Fowler et al., 2019c) and of the Mary Bay vent fluids (Gemery-Hill et al., 2007). Vent fluid data from Fowler et al. (2019a, 2019c) are plotted for comparison and show that data for the vapor-dominated Deep Hole fluids plot mostly in the kaolinite and boehmite fields and are silica-undersaturated whereas the alkaline-Cl SE-WT fluids plot near the smectite (Mg-beidellite) and chlorite (daphnite) fields and are oversaturated with quartz.

Inferred conditions of hydrothermal alteration in the pre-explosion hydrothermal systems at Mary Bay and Elliott's Crater, at and beneath the lake floor, are highlighted on Figure 14 at temperatures up to 300 °C and at SiO₂ activity overlapping the quartz and amorphous silica saturation boundaries. The temperatures of likely pre-explosion alteration are based on fluid inclusion studies of lithic fragments in Mary Bay breccia that indicate temperatures of 228-294 °C for liquid inclusions with significant Cl and low CO₂ content (Morgan et al., 2009). The temperature range of alteration from ~125–300 °C (Fig. 14) also is consistent with inferred or measured temperatures beneath subaerial hydrothermal systems throughout Yellowstone (Fournier, 1989; Hurwitz and Lowenstern, 2014). Preexplosion alteration is inferred in the daphnite (chlorite) and Mg-saponite (smectite) stability fields and agrees with abundant Mg-Fe chlorite and Mg-Fe smectite minerals found in both the Mary Bay and Elliott's Crater hydrothermal explosion deposits (Fig. 10).

Small Hydrothermal Explosion Events

Vapor-dominated systems contain highenthalpy steam and non-condensable gases (especially CO₂ and H₂S) and can create explosions by sudden vapor expansion but lack the expansive power of alkaline-Cl liquids that flash to steam. Vapor-dominated systems are more likely to produce smaller explosions. For example, Montanaro et al. (2016a) performed rapid decompression experiments under controlled laboratory conditions that mimic hydrothermal explosion conditions using host rocks from the 2012 Te Maari hydrothermal explosion in the Tongariro volcanic field, New Zealand. The experiments showed that flashing (sudden boiling and expansion of liquid water) produced about an order of magnitude more energy (2.2-6.5 kJ/kg) than simple one-phase steam expansion (0.2-0.9 kJ/kg).

As many as 14 less-extensive, smaller volume hydrothermal explosion deposits are present in the cores (Figs. 4A and 4B). At least 11 small-volume, relatively thin, fining-upward deposits

occur in cores YL16-3A, YL16-5A, and YL92-3A (Figs. 4A and 4B), and deposits from three small explosion events are present in the shorter gravity cores (Fig. 12). Most likely, these deposits represent localized hydrothermal explosion events. The small explosion deposits in YL16-3A and YL16-5A were likely sourced at the vapor-dominated Deep Hole vent field ~200 m north of YL16-3A; ~2.4 km west of YL16-5A) and likely formed from sudden vapor-expansion explosions. Assuming sedimentation rates of \sim 1.06 m/k.y. (Fig. 5), the ages of the smaller deposits in core YL16-3A are ca. 6.5 ka, ca. 5.8 ka, ca. 5.1 ka, ca. 2.4 ka, and ca. 2.0 ka. Primary fall (facies fBr) or remobilized (facies fss) hydrothermal explosion deposits in core YL16-3A may have been transported directly south from the Deep Hole (Figs. 1 and 3C). Likewise, in core YL16-5A, the smaller events occurred at ca. 5.4 ka, ca. 2.4 ka, and ca. 1.1 ka. Possible correlation of events at ca. 5.6 ka and ca. 2.4 ka strengthens the assertion of a common source from the Deep Hole.

Three small hydrothermal explosion deposits occur in core YL92-3A in the West Thumb basin at 3.01 m, 6.48 m, and 8.81 m depths, but the sources of the deposits are unresolved. Given the estimated lake sedimentation rate in the West Thumb basin (1.04 m/k.y.) (Fig. 5), we infer that the ages of the small hydrothermal explosion deposits are ca. 8.8 ka, ca. 6.5 ka, and ca. 3 ka. The 1-cm-thick unit at 6.48 m in YL92-3A is at the same stratigraphic position as a 5-cm-thick unit (6.41-6.46 m) in YL16-3A (17 km away), but additional work is needed to determine possible correlation. Two large explosion craters, the subaerial Duck Lake crater northwest of the West Thumb Geyser Basin and the subaqueous Evil Twin crater east of Duck Lake (Fig. 1) are in the general location of core YL92-3A, however, the ages of the Duck Lake and Evil Twin explosions are unknown. Seismic-reflection profiles from West Thumb basin near core YL92-3A (Tiller, 1995; Morgan et al., 2007b) show numerous hydrothermal domes, gas pockets, hydrothermal vents, and areas of high attenuation in the shallow subsurface, which raises the possibility of small, local vapor-expansion explosions.

Large Hydrothermal Explosion Events

The Elliott's Crater Hydrothermal Explosion Front

The 8 ka Elliott's Crater event was a massive hydrothermal explosion; its deposits are widely distributed throughout Yellowstone Lake in 10 sediment cores (Figs. 4 and 8). They are moderately to well sorted, normally graded, and hydrothermally altered sequences (Fig. 9B), indicating deposition of ejecta through the water column.

Additionally, the lack of a significant ejecta apron around Elliott's Crater substantiates this system as entirely subaqueous when it exploded and suggests that most of the local breccia fall-out from the primary explosion was dispersed by wave and water action.

The Elliott's Crater hydrothermal explosions, driven by flashing of alkaline-Cl hydrothermal liquids to steam, started near the surface and descended into the subsurface to a depth where the hydrothermal system was depleted of steam. Hydrothermal explosions involving liquid flashing to steam are top-down explosions with the near-surface material ejected first and the deepest part of the system ejected last in each explosion cycle or pulse (Fig. 15; Browne and Lawless, 2001; D'Elia et al., 2020; Gallagher et al., 2020; Mastin, 1991; McKibbin, 1990; McKibbin et al., 2009; Smith and McKibbin, 2000; Montanaro et al., 2020b; Morgan et al., 2009). Elliott's Crater is still active; in fact, large (30 to 80 cm diameter), subrounded rocks on the surficial sediments of the southeast crater rim (Fig. 3D) suggest that explosions are continuing to recent times.

Features of the Elliott's Crater hydrothermal explosion deposits (Figs. 7, 8, and 9B) relate directly to explosion processes. Multiple sequences of the primary fall facies (cBr, fBr) from Elliott's Crater are present in cores. In general, the first explosions were the most intense, voluminous, and powerful. Each subsequent explosion decreased in intensity as reflected by smaller clast size and thinner primary deposits. Some deposits include suspension-fallout deposits (facies msm), suggesting a time gap represented by a suspension fallout deposit between deposition of two primary fall explosion deposits. Deposition of coarser deposits is instantaneous compared to the delayed deposition of the suspension fallout deposits, which represent the very fine-grained sediment from the explosion suspended in the water column after an explosion event.

Cores YL16-4A and YL16-4C in Elliott's Crater are unique. They contain the thickest, most highly altered breccia deposits, which fell back into the source crater and represent the most proximal deposits observed in any of the cores. The intracrater debris at the base of the two cores records early explosions containing multiple pulses of predominantly highly altered clay. The final phase of these early explosions deposited alternating beds of altered gray clay and black obsidian sand. The matrix-supported, hydrothermally altered, medium-gray, clay-rich mud contains abundant clasts of angular-to-subangular, white chlorite-rich clay interbedded with obsidian-rich sand layers. We interpret this as representing pulsations in the explosion column. The largest white clay clasts are in the basal parts of

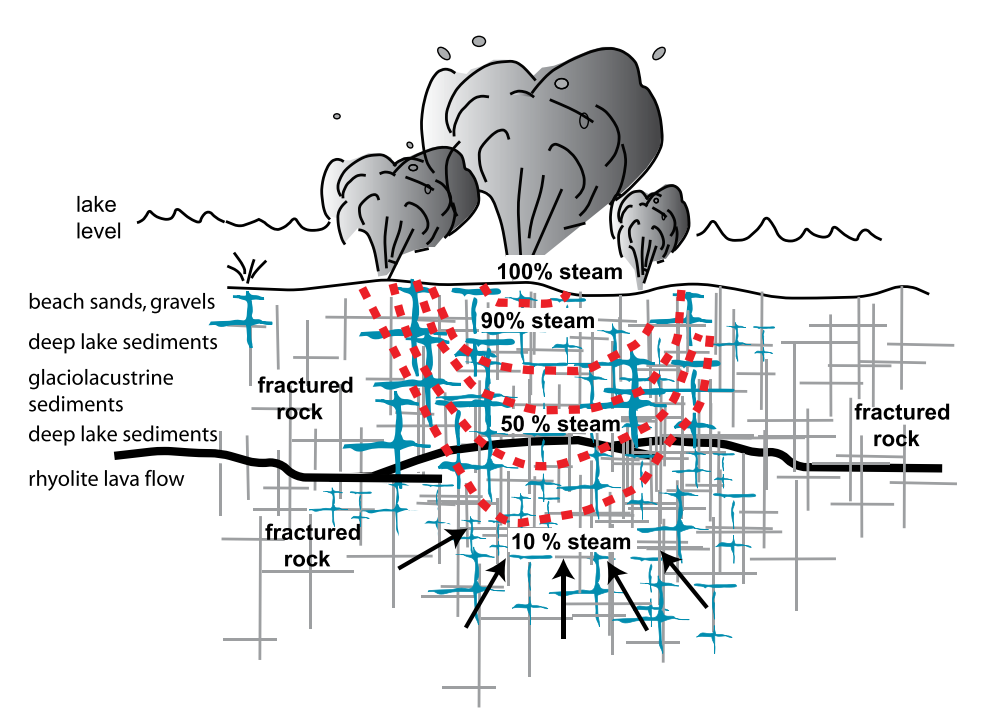


Figure 15. Schematic diagram illustrating a large hydrothermal explosion in Yellowstone Lake (Wyoming, USA) generated by a sudden pressure drop at the surface, which allows alkaline-Cl liquids at the boiling point to flash to steam. This pressure drop is transmitted downward through hydraulically connected fractures, starting a series of instantaneous and cascading explosions that result in the expulsion of large amounts of fractured rock, altered clay, boiling muds, and water and steam, and the production of a large crater. As the pressure drop propagates to depth, a progressive decrease in the amount of steam is produced until, at some depth, no steam is produced. The magnitude of the pressure drop relative to the boiling curve determines the percentage of steam produced. Included on diagram is a schematic subsurface stratigraphy beneath the Mary Bay explosion crater including, from the subsurface down, silicified beach sands and gravels, silicified pebble conglomerates, silicified layered beach sand/pebble conglomerates, chalcedonic pebbles, sulfidic gravel conglomerates, silicified lake sediments, multigenerational silicified breccia clasts and chalcedonic breccia, and hydrothermally altered, quartz-phyric rhyolite clasts containing open vugs lined with bipyramidal quartz crystals with secondary hydrothermal quartz overgrowths, calcite crystals, zeolites, and cubic pyrite crystals (figure modified from Morgan et al., 2009). The fine-grained sand-and-silt deposits, exposed immediately below the Mary Bay explosion deposit and interpreted as tsunami-related deposits, are not included in diagram as they were not in the subsurface and are interpreted as being deposited on the surface immediately prior to the Mary Bay hydrothermal explosion.

core YL16-4C. The primary fall deposits in cores YL16-4A and YL16-4C also contain fragments or rounded aggregates of hydrated black obsidian, white sinter, broken fragments of crystals, and brown clay. The presence of this assemblage is consistent with a pre-explosion, alkaline-Cl, silica-depositing hydrothermal system.

Additional explosion deposits likely occur below the base of each of the cores in Elliott's Crater. Crater excavation depths are much deeper than post-eruptive craters given that the craters are refilled by ejecta falling back into the crater as evidenced in cores YL16-4A and YL16-4C. Systems the size of Elliott's Crater commonly eject fragments exceeding diameters of 1 m

(Browne and Lawless, 2001), however, clasts of this dimension are not present in the cores inside Elliott's Crater, strongly suggesting coarser breccia fragments are at greater depths.

Deposits in core YL16-5A (Fig. 7A) contain an abundance of altered rhyolite fragments at the base of the Elliott's Crater explosion deposit. The Elliott's Crater deposits in core YL16-5A likely were excavated from deeper levels in the subsurface than those observed in cores YL16-4A and YL16-4C from Elliott's Crater. The evidence of rhyolite-rich accumulations in the explosion deposits suggests that the clasts were excavated from the top of an unmapped rhyolite lava flow at depth (Fig. 15) and fell to the base

of the sequence due to the size and greater density of fragments that settled rapidly through the water column.

Finally, we hypothesize later explosions originated from the smaller but significant secondary crater in the southeast part of Elliott's Crater and produced the hummocky breccia lobe, that extends 2.6 km south-southeast of the crater and is estimated to be \sim 10 m thick and 0.4 to 0.6 km wide (Figs. 3D and 16A). Seismic-reflection profiles of this lobe indicate 4-7.5 m of postexplosion lacustrine sediments overlie a strongly attenuated deposit, interpreted as a resistant breccia deposit that formed synchronously or not long after the main Elliott's Crater eruption (Johnson et al., 2003). This later stage of directional venting is substantiated by the fact that the southern rim of Elliott's Crater is embayed and 8-10 m lower than the northern crater rim, consistent with a lateral or directed blast of the explosion.

Elliott's Crater explosion deposits in the sediment cores become progressively thinner with distance from the crater to the south, east, and west in the lake (Fig. 16A). Alternating obsidian and clay layers present in the basal Elliott's Crater explosion deposit sequences in core YL16-3A (Fig. 9B) may represent earlier phases of the explosion directed to the southwest, possibly by prevailing winds.

The estimated total volume of explosion deposits ejected from the crater is 0.07 km³ (Table S4), based on the distribution and thickness of deposits in the sediment cores plus the estimated volume of the hummocky deposits southeast of the crater. The volume of the present-day 40-mdeep Elliott's Crater is 0.02 km³, but it is partially to substantially refilled with intracrater fallback deposits, as observed in cores YL16-4A and YL16-4C. The total depth of excavation is unconstrained, but the total volume of ejecta erupted suggests the crater had to be ≥180 m deep (Table S4). The energy released by the entire Elliott's Crater explosion is estimated at 0.4- 0.9×10^{15} J based on a comparison to experimental data on rocks from the Te Maari (New Zealand) hydrothermal explosion, which gave a range of energy produced of $0.5-1.3 \times 10^7$ J/m³ for liquid flashing to steam in rocks with 7%-26% porosity, respectively (Montanaro et al., 2016a).

Triggers for the Elliott's Crater hydrothermal explosion. Bathymetric, stratigraphic, and hydrothermal evidence supports the inference that Elliott's Crater was a large hydrothermal dome prior to its explosion. Seismic-reflection profiles across the crater show that layered lake sediments are conformably upwarped on its southern slope (Fig. 3D; Johnson et al., 2003) and suggest that hydrothermal doming occurred prior to the hydrothermal explosion event.

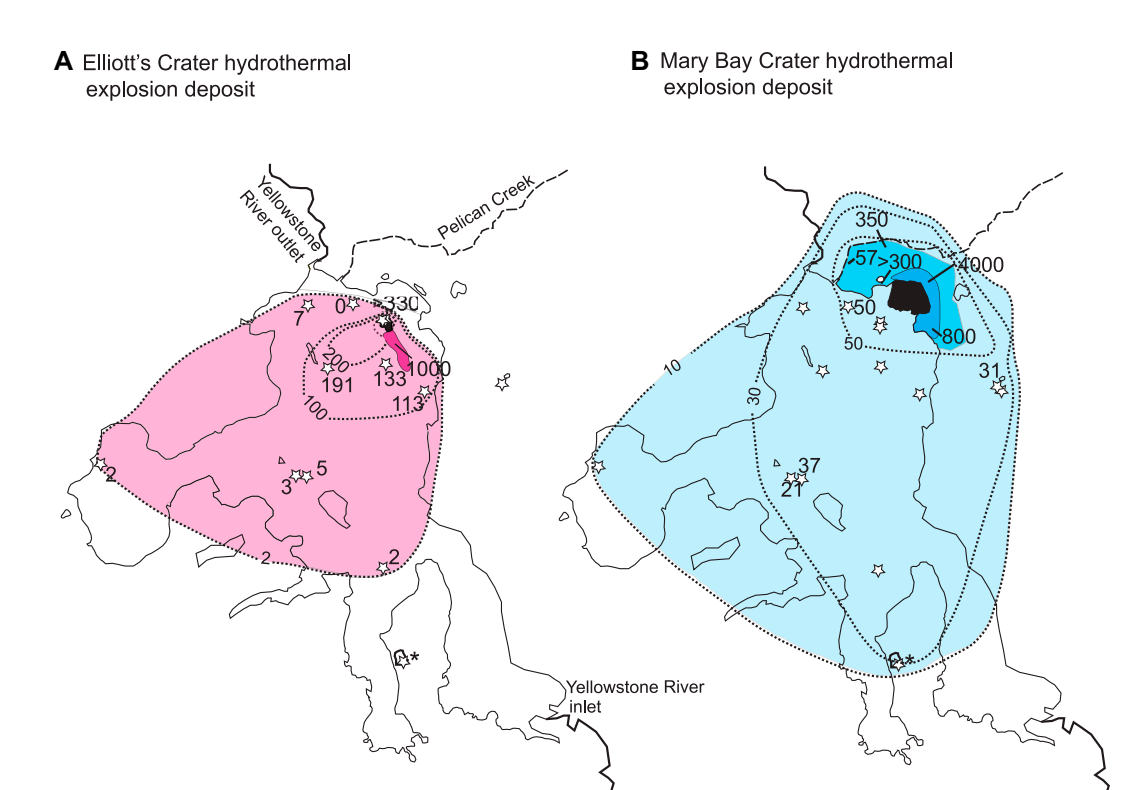


Figure 16. Areal distribution and thickness (in cm) of hydrothermal explosion deposits from (A) Elliott's Crater and (B) Mary Bay explosion craters in Yellowstone Lake area (Wyoming, USA). White stars represent the 2016, 1992, 2017, and Alder Lake piston cores collected from Yellowstone Lake and Cub Creek Pond. Yellowstone River at the north end at Fishing Bridge is the only outlet of the lake. (A) Distribution of the Elliott's Crater hydrothermal explosion deposit is shown in magenta shading. Black represents crater area of Elliott's Crater; light magenta is the approximated extent of Elliott's Crater explosion deposit in Yellowstone Lake. Dashed black lines represent approximated thicknesses (isopleths in cm) of Elliott's Crater deposit. A medium magenta (~1000-cmthick) lobe of explosion breccia

extends south-southeast from the crater and is interpreted as a later directed blast from the subcrater in the southern portion of the main crater (Fig. 3D). (B) Distribution of the Mary Bay hydrothermal explosion deposit is shown in cyan shading. Black represents the Mary Bay crater, medium cyan represents Mary Bay explosion deposits exposed on land, medium-dark cyan represents the crater rim on land, and light cyan represents approximated distribution of the Mary Bay explosion deposit in the Yellowstone Lake and Cub Creek Pond areas. Isopleths indicate 50, 20, and 10 cm thickness in cores and are used to calculate the volume of Mary Bay deposits in and around the lake. The West Thumb data for YL92-3A are based on seismic-reflection profile interpreted to include a reflector at ca. 13 ka (Tiller, 1995).

In Yellowstone Lake, hydrothermal domes occur where impervious, diatom-rich lake sediments are arched upward by underlying pockets of gas or gas-charged fluids (Johnson et al., 2003; Morgan et al., 2007b). The hydrothermal fluids may be vapor-dominated or alkaline-Cl liquids that are exsolving vapor on ascent. Many domes in Yellowstone Lake have a hardened (semi-lithified) cap, as reflected in multibeam sonar backscatter images from the lake (Morgan et al., 2007b), and are composed of clay minerals, including smectite and chlorite (Shanks et al., 2005, 2007) and/or silica (Morgan et al., 2009). Buoyant thermal fluids that rise in a plume through porous lake sediment cause hydrothermal alteration and decreased permeability, increased pore pressure, and increased strength (Heap et al., 2021; Mordensky et al., 2018; Passaro et al., 2016; Pickrill, 1993). The alteration and resulting reduction in permeability can inhibit fluid circulation creating zones of high pore fluid pressure (Heap et al., 2021) causing doming or deformation of the sediments. If fluid flow is focused where pore fluid pressure exceeds the confining pressure or strength of the overlying impervious caprock, a rapid decrease in pressure could convert reservoir liquid to steam, changing the pressure gradient within the reservoir from hydrostatic to vaporstatic, overpressurizing the reservoir top and initiating brecciation (Jamtveit et al., 2004), which would lead to a hydrothermal explosion (Mastin, 1995; McKibbin et al., 2009). The ratio of high pore fluid pressure relative to confining pressure defines the susceptibility of the edifice to failure (Day, 1996). Collapse of volcanic edifices is analogous and can be triggered by a variety of mechanisms often associated with igneous intrusions, including degassing (Day, 1996), deformation associated with faulting and seismic events, and heating of confined pore fluids. It follows that similar conditions could lead to the collapse or explosion of hydrothermal domes, especially those with impervious silicified or clay (smectite, chlorite) caps. Active hydrothermal domes also may be disrupted by seismic events that rupture the cap.

Seismic-reflection profiles show that the Eagle Bay fault system in the southern part of the lake between Snipe Point and Frank Island (Figs. 1 and 13B) experienced \sim 2.8 m of dis-

placement at ca. 8 ka. Similarly, a smaller faultdisplacement event at the Lake Hotel graben near the northern reach of the fault zone likely correlates with the Elliott's Crater explosion at 8 ka, based on sedimentation rates (Figs. 5 and 13A). Core YL16-6A contains a distinct slump deposit on the steep eastern shore of Yellowstone Lake that incorporated significant material from the Elliott's Crater explosion. Large fragments of white, chlorite-rich clay (Fig. 7C) within a mud slump sequence at 7.02-7.61 m depth in core YL16-6A are similar to Elliott's Crater deposits in cores YL16-3A, YL16-4A, YL16-4C, and YL16-5A. We suggest this distinct slump formed due to seismicity from synchronous fault displacement events along the Eagle Bay fault zone. We also suggest the white, chloriterich clay fragments, concentrated in the lower portions of the Elliott's Crater deposit, represent ejected remnants of the capping dome.

Lake level at ca. 8 ka was \sim 5 m above present-day lake level, based on radiocarbon ages of shoreline terraces (Pierce et al., 2007). This suggests that any sudden decrease in lake level would be restricted to a few meters and would be

an unlikely trigger for a major hydrothermal explosion because of the small pressure change involved (\sim 0.3 atm). Possible tsunami waves over Elliott's Crater generated by the fault displacement probably also would only have produced small transient pressure changes.

The geologic evidence suggests a continuous cap on the hydrothermal dome over the Elliott's Crater hydrothermal system at 8 ka and the inferred presence of pressurized, ascending alkaline-Cl hydrothermal fluids beneath the capped dome. Given this setting, the most likely trigger for this major hydrothermal explosion was the significant fault displacement event along the Eagle Bay fault zone and related paleoseismicity that fractured the dome and initiated a top-down explosion by flashing liquid fluids to steam due to pressure release.

The Mary Bay Hydrothermal Explosion Event

The 13 ka Mary Bay deposits are recognized in five cores (YL16-1A, YL92-1A, YL92-1C, CUB17-1A, CUB17-1B) and likely were present in a sixth sediment core from Alder Lake (Tiller, 1995; Sherrod, 1989; Figs. 1, 4A, and 4B). Furthermore, Tiller (1995) speculated that a prominent reflector in the seismic section taken near core YL92-3A in the West Thumb basin represents the Mary Bay deposit there, although the core did not penetrate this horizon. The Mary Bay explosion deposits originate from an enormous hydrothermal explosion crater (\sim 2.5 km diameter) that contains a complex of smaller craters that are hydrothermally active today with temperatures of ≥120 °C. Most vent-fluid compositions in Mary Bay are alkaline-Cl (Fig. 3F) with a few vents being vapor rich, which probably represent vapor boiled from the ascending alkaline-Cl fluid (Balistrieri et al., 2007; Gemery-Hill et al., 2007).

The Mary Bay hydrothermal explosion produced Earth's largest documented hydrothermal explosion crater (Browne and Lawless, 2001), the most voluminous hydrothermal explosion deposit known, and has the greatest areal extent of any such documented deposit. Modeling of the atmospheric column height (Mastin, 2001, 2007) produced by this event suggests a height of 2 km (Morgan et al., 2009). Distribution patterns of the explosion deposits (Fig. 16B) indicate that the finer grained explosion sediments were dispersed to the south-southwest in the lake, possibly due to prevailing wind. Thick, coarse subaerial breccia deposits north and northeast of the Mary Bay crater indicate a near-vertical ejection angle (Morgan et al., 2009).

Measured sections of explosion deposits on land from the Mary Bay crater indicate thick, poorly sorted, and matrix-supported deposits (Fig. 9A) and represent features that unambiguously indicate rapid subaerial deposition (Browne and Lawless, 2001; Morgan et al., 2009). Wave-cut cliffs 6-7 m high along the northern lakeshore expose individual silicified clasts, ranging up to 2-3 m in maximum length, that are scattered through a fine-grained, hydrothermally altered, clay-rich matrix. The northeast ejecta rim, \sim 300 m north of the lakeshore, is 37 to 46 m high. Measured sections to the north and east of the lake show breccia deposit thicknesses of 3-40 m. Between Holmes Point and Steamboat Point (Figs. 1 and 16B), deposits within the southeast crater rim onlap the Steamboat Point thermal kame deposits. No rim is present in the now-subaqueous southern part of the Mary Bay crater.

The Mary Bay explosion occurred in an extensive, hot, active, probably long-lived, hydrothermal system. Lithic clasts in the Mary Bay breccia, exposed in onshore outcrops adjacent to the western margin of the Mary Bay crater, have a wide range of compositions (Morgan et al., 2009, Fig. 15). Clasts excavated during explosion events from shallower environments include wet clasts of fine-grained sand, and hard, silicified beach sands to gravels, and silicified lake sediments (some with pyrite veins). Clasts from deeper in the subsurface include silicified multigenerational breccia clasts and chalcedonic breccia. The deepest inferred source environment is represented by abundant (\sim 25% of all clast lithologies), hydrothermally altered, silicified, quartz-phyric rhyolite and brecciated rhyolite clasts, many of which contain open vugs lined with bipyramidal quartz crystals that locally have secondary overgrowths, calcite crystals, zeolites, and cubic pyrite crystals. We suggest the quartz-phyric rhyolite was excavated from a previously unknown flow unit not mapped in surface exposures (Morgan et al., 2007a, 2007b, 2009). Many clasts from deep environments have thermal cracks on surfaces. Interpreted variations in depths of lithic clast compositions in hydrothermal explosion breccias are inferred to be associated with a rapid top-down sequence of hydrothermal explosive activity from shallow levels in the system to depths >180 m (Morgan et al., 2009).

The Mary Bay explosion deposits in the cores, in contrast with the subaerial deposits, are well-sorted, fining-upward sequences (Figs. 1, 9A, and 16B; Table 2). Based on the number of proximal primary fall sequences (facies *cBr*), cores more proximal to the Mary Bay crater (YL16-1A, CUB17-1B, CUB17-1A) record at least three pulses in the explosion, which occurred in rapid succession. The *cBr* facies deposits are coarse, well sorted, fine upward, and lack intercalated suspension fallout deposits (facies *msm*; Table 2). Farther from the Mary Bay crater

source (YL92-1A, YL92-1C), the deposits are finer grained (facies *fBr*) with explosion pulses separated by 7–10 cm of suspension-fallout deposits (facies *msm*, Figs. 4A, 4B, and 8).

Further evidence of the power of the Mary Bay explosion is exemplified by fractures filled with coarse, unsorted, hydrothermally altered explosion breccia that crosscut lake sediments below the Mary Bay deposit adjacent to the western crater wall along the northern shore of Yellowstone Lake (Fig. 9A). Hydrothermally altered, but finer-grained, silt-filled fractures crosscut faulted lake sediments in core YL92-1A adjacent to the Eagle Bay fault zone ~13.7 km from the Mary Bay crater (Figs. 1 and 9A). We interpret the silt-filled fractures below the Mary Bay deposit and 4 cm above the Glacier Peak ash as hydrothermal explosion breccia injected as dike-like features into then-shallow depths within soft lake sediment, synchronous with Mary Bay seismic and explosion events.

New findings herein show that the volume and areal extent of the Mary Bay deposit is significantly greater than previous estimates (Morgan et al., 2009). The sublacustrine Mary Bay explosion deposits, based on thicknesses and distribution in the Yellowstone Lake cores, cover an estimated area of ~390 km² and comprise an estimated volume of \sim 0.14 km³ (Fig. 16B; Table S4). The thick onshore deposits north and east of the lake are estimated to cover a total area of \sim 20 km² with approximated explosion deposit thicknesses from 3 to 40 m, indicating an onshore volume of ~ 0.13 km³. Explosion deposits onshore and offshore have an estimated total volume of ~0.27 km³, which requires a full crater eruption depth of at least 225 m, using the measured crater area of 3.57 km² and a conical excavation volume (Fig. 16B; Table S4). A similar volume calculation using only the area of the inner crater (Fig. 3E; 1.9 km²) suggests a depth of 420 m for a conical excavation volume. Both depth estimates are reasonable given the fluid inclusion data (Morgan et al., 2009) that indicate temperatures between 228 °C and 294 °C and entrapment of fluids at depths between 180 m (lithostatic pressure) and 540 m (hydrostatic pressure). The estimates of excavation volume, depth, and energy are probably minimums because they do not include breccia that was ejected and fell back to substantially refill the crater. Energy exerted in the Mary Bay explosion is $\sim 1.3-3.5 \times 10^{15} \text{ J}$, based on the estimated volume of $\sim 0.27 \text{ km}^3$ and using energy-volume relationships developed by Montanaro et al. (2016a) for the Te Maari (New Zealand) system for rocks with 7%-26% porosity. Mary Bay produced a total energy and volume roughly four to six times that of Elliott's Crater.

Triggers for the Mary Bay hydrothermal explosion event. The Mary Bay explosion may

represent the culmination of several significant geologic events after retreat of the >1-km-thick, Pinedale-age ice cap at ca. 15–14.5 ka (Licciardi and Pierce, 2018). We hypothesize that the 13 ka Mary Bay hydrothermal explosion was triggered by a sequence of events that led to a sudden drop in lake level.

The 13 ka seismic event of the Lake Hotel graben resulted in a net slip of 95 cm and is estimated as a magnitude 5.3 or greater event (Johnson et al., 2003). Empirical relations of historic earthquake magnitudes to the rupture lengths (Wells and Coppersmith, 1994) indicate that the rupture length related to this displacement must extend beyond the Lake Hotel graben farther south on the 25-km-long Eagle Bay fault zone (Fig. 1) as well as to the north. A seismic-reflection profile from Snipe Point in the south-central lake shows synchronous offsets of up to \sim 1 m (Figs. 1 and 13) at ca. 13 ka (Fig. 5). A rupture of this length could have generated an estimated magnitude 6.5 earthquake (Johnson et al., 2003) and contributed significantly to events at 13 ka, including generation of a tsunami.

Tsunami occurrences in lakes due to earthquakes and fault displacement are well documented and, increasingly, are recognized in large lake environments (Kremer et al., 2012, 2021; Moore et al., 2014; Nigg et al., 2021; Smoot et al., 2000). Morgan et al. (2009) hypothesized that the onshore distribution and physical characteristics of obsidian-rich sand-and-silt deposits (facies bfss, Figs. 4A and 4B), some containing small en echelon displacements, that occur immediately below and in contact with the Mary Bay explosion breccia, are the product of a tsunami. The obsidian-rich sand units occur along the northern shore of the lake and in stream channels north of the lake where the deposits show lateral variability in bedding, grain size, and thickness due to higher energy conditions (Morgan et al., 2009).

Along the northern shore of the lake, clasts (up to 8 m long) of unconsolidated, bedded sand, identical in appearance to the sands below the Mary Bay deposit, are incorporated as breccia clasts into the overlying lower units of the Mary Bay explosion deposit (Fig. 9A). We infer that the sand clasts are from the tsunami unit deposit emplaced after the initial seismic event. We further propose that the upper sand layer was entrained into the early and proximal Mary Bay explosion deposits as wet, cohesive sand units. Unlike the other clasts in the Mary Bay deposit that are silicified and mineralized, the exposed sand clasts deposits today are friable and soft and could not have been transported in their current state. We note the sand clasts are present only in the lowest/earliest phase deposits of the Mary Bay deposit adjacent to the western crater rim,

which is consistent with a top-down explosion path (Fig. 15).

In cores YL16-1A, YL92-1A, and YL92-1C, the tsunami-related deposits occur as a bedded, normally graded, fine-grained sand-and-silt sequence (facies *bfss*), below and in contact with the Mary Bay breccia and are finer grained and more uniform than stratigraphically correlative sands exposed on land. Whereas much of the entrained sediment in the inferred wave was deposited on land (Morgan et al., 2009), we assume some material also was suspended in the lake-water column following the tsunami event and settled over time.

The Eagle Bay-Lake Hotel seismic event and subsequent tsunami likely contributed to a significant drop in lake level due to rapid erosion of the Yellowstone Lake outlet channel. Lake-level estimations (Pierce et al., 2007) suggest that at 13.6 ka, before the Mary Bay explosion, Yellowstone Lake level was $\sim 15 - \sim 17$ m above present lake level. Radiocarbon ages from an incised stream channel north of the lake and from bluffs along the northern lakeshore give ages of ca. 13.4 and ca. 12.9 ka at ~ 2.9 m and ~ 3.6 m above present

lake level, respectively (Pierce et al., 2007; Richmond, 1976, 1977). Taken together, these ages approximate the timing of both the hydrothermal explosion and the tsunami event and indicate elevations that are $\sim\!\!3$ m above present-day lake level, consistent with a rapid $\sim\!\!14$ m drop in lake level and subaerial deposition of the Mary Bay hydrothermal explosion breccia north of Yellowstone Lake. These data also are consistent with the Mary Bay explosion deposits in the cores.

Seismicity of a magnitude 6.5 earthquake (Johnson et al., 2003) and fault displacement at ca. 13 ka could have triggered the Mary Bay explosion directly or contributed to a lake outburst flood by disrupting glacial deposits mapped north of present-day Yellowstone Lake near Le-Hardy's Rapids (Richmond, 1976, 1977). The tsunami immediately preceding the Mary Bay explosion may have acted in tandem with the seismic event to help trigger the hydrothermal explosion. We hypothesize that the tsunami was funneled into Yellowstone River at Fishing Bridge gaining depth and erosive power through the narrow, <1-km-wide gap at LeHardy's Rapids (Fig. 17) and eroding glacial kame and

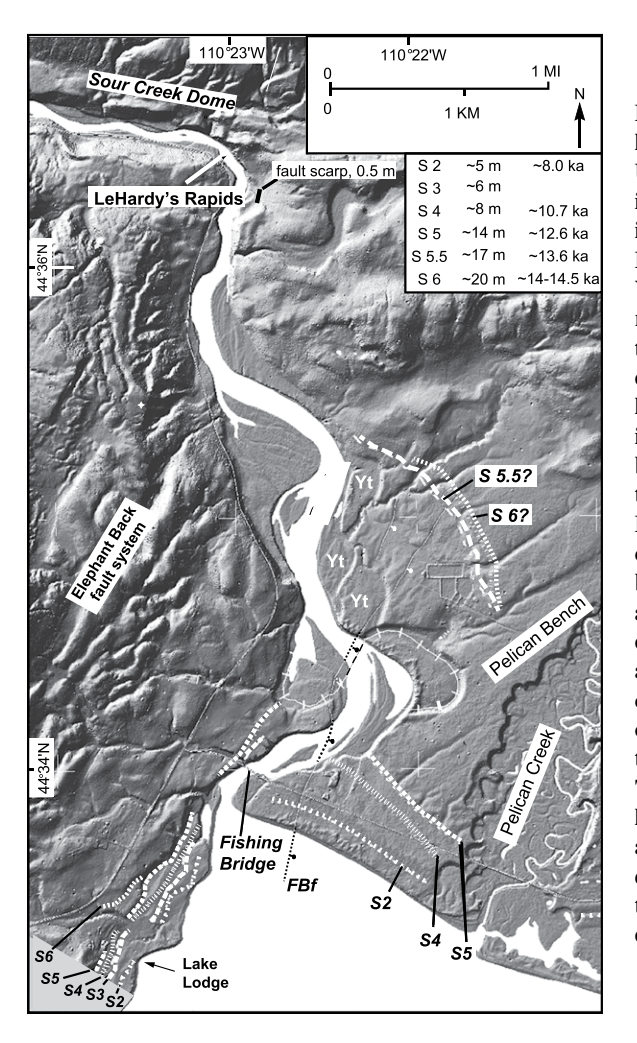


Figure 17. LiDAR map of Yellowstone River area (Wyoming, USA) from its outlet at Fishing Bridge to LeHardy's Rapids (after Pierce et al., 2007). FBf—Fishing Bridge fault; Yt-Yellowstone River terraces: S2-S6—shorelines. Note that shorelines S5.5 and S6 are exposed along east side of Yellowstone River valley, indicating a higher lake level shortly before the Mary Bay hydrothermal explosion. The 13 ka Mary Bay event deposited coarse, poorly sorted explosion breccia in a subaerial setting along the northern and eastern shores of Yellowstone Lake and well-sorted explosion breccia in fining-upward sequences observed in piston cores from the sublacustrine environment. This contrast suggests that the lake level dropped to within a few meters of the presentday lake level at the time of the Mary Bay hydrothermal explosion.

Summary of Events in Yellowstone Lake

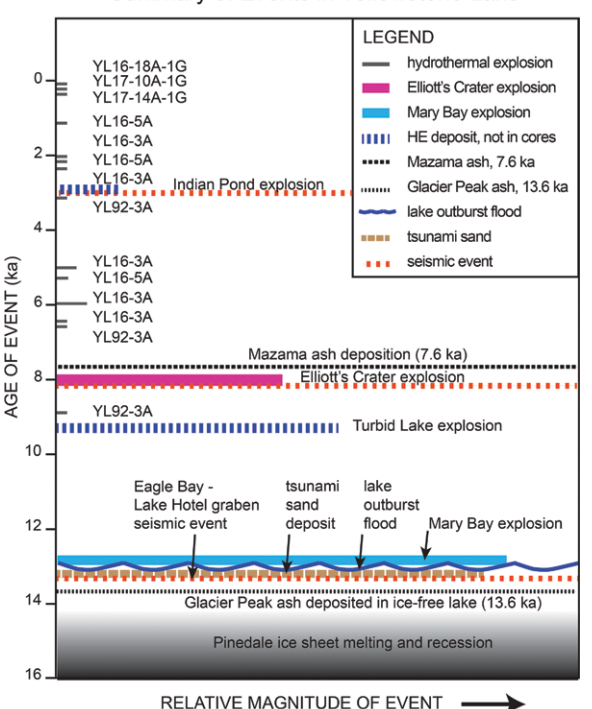


Figure 18. Representation of approximate volume or relative magnitude of known hydrothermal explosion deposits versus age over the last 14 k.y. Four very large hydrothermal explosions occurred in the northern Yellowstone Lake area (Wyoming, USA) during this period. The huge Mary Bay explosion occurred shortly after recession of the Pinedale ice sheet and is closely related to (1) a major seismic event along the length of the Eagle Bay fault zone (including initial formation of the Lake Hotel graben) that led to (2) a lake-wide tsunami that deposited a bedded fine sand-and-silt deposit that immediately underlies the explosion deposit throughout the lake, (3) a lake outburst flood that breached recessional moraines at LeHardy's Rapids and suddenly lowered the lake

level by ~14 m, and (4) explosion of the Mary Bay hydrothermal crater. The Elliott's Crater and Indian Pond hydrothermal explosion events are roughly correlated with younger fault displacement events in the Eagle Bay fault zone and the Lake Hotel graben. Smaller, younger explosion deposits are likely derived from vapor-dominated steam expansion eruptions. At least 16 hydrothermal explosions have occurred in Yellowstone Lake over the past 13 k.y. as evidenced in the lake cores. HE—hydrothermal explosion deposit.

till deposits on the valley floor (Pierce et al., 2007; Richmond, 1976, 1977). We infer that this caused a substantial outburst flood that rapidly lowered lake level by \sim 14 m and resulted in a hydrostatic pressure reduction of at least \sim 1.4 atm over an active, well-established, sublacustrine hydrothermal system in Mary Bay, thus triggering the explosion (Fig. 18).

Comparable events are well known in the historical and geologic record. Strasser et al. (2008) estimated that a moraine dam breach and lake outburst flood on Lake Zurich, Switzerland at 13.76 ka drained 2.5 km³ of the lake water and lowered the lake level by \sim 12 m in \sim 7–19 days. An \sim 14 m drop in Yellowstone Lake level amounts to $\sim 5 \text{ km}^3$ of lake water but direct comparison is difficult. Similarly, the modern ice-dammed Gengissig Lake, Iceland and Lake Okaro, Taupo Volcanic Zone, New Zealand (Montanaro et al., 2016a, 2016b) experienced outburst floods that triggered hydrothermal explosions. Muffler et al. (1971) proposed that a lake outburst process may have triggered the large Pocket Basin hydrothermal explosion in Lower Geyser Basin, YNP.

We conclude that the principal cause of the Mary Bay explosion was the sudden and significant pressure decrease due to rapid lake level drop triggering top-down flashing of alkaline-Cl fluids to steam over a temperature range from $\sim\!300$ to $100~^\circ\mathrm{C}$ in an explosion that excavated the world's largest explosion crater and produced the world's most voluminous explosion deposits.

CONCLUSIONS

At least 16 hydrothermal explosion deposits are recorded in 17 of 18 lake sediment cores from Yellowstone Lake ranging in age from 13 ka to \sim 1860 CE (Fig. 18). Among these explosions, the 8 ka Elliott's Crater and 13 ka Mary Bay crater explosions represent extreme hydrothermal explosion events; deposits from both events are distributed extensively in the lake basin and at least one is present in 14 of the sediment cores. Smaller hydrothermal explosion deposits, having a more limited areal extent, are present in six cores. The youngest explosion deposit is at \sim 15 cm depth (\sim 1860 CE) in core YL16-18A-1G from the Deep Hole (Figs. 3C

and 18), an active, vapor-dominated (H₂O, CO₂, H₂S) hydrothermal system.

Yellowstone Lake hydrothermal systems are characterized by either alkaline-Cl fluids or by vapor-dominated fluids. Predominance of chlorite, smectite, and amorphous silica alteration characterizes hydrothermal explosions related to alkaline-Cl fluids whereas kaolinite alteration characterizes explosions related to vapor-dominated systems. Alkaline-Cl liquids flash to steam during hydrothermal explosions, producing much more energetic events than sudden vapor expansion in vapor-dominated systems. This relationship between alkaline-Cl fluids versus vapor-dominated fluids may prove critical in assessing the magnitude of potential future hydrothermal explosions.

Explosion deposits interbedded in lacustrine sediments are distinct due to mineralogical and chemical signatures of the pre-explosion hydrothermal alteration. Physical sorting of the explosion deposits in the sediment cores indicates that the explosion ejecta fell through the water column, as evidenced by the presence of normal grading and clay-to-pebble-sized dropstones within basal layers. Six hydrothermal explosion facies are recognized in the cores and detailed stratigraphic analysis of the explosion deposits indicates that both the Mary Bay and Elliott's Crater explosions consisted of multiple pulses.

The initial and strongest explosions of Elliott's Crater and Mary Bay produced extensive deposits and were top-down explosion events. The explosion from Elliott's Crater may have been directed to the south, whereas deposition of the Mary Bay explosion deposit suggests a near-vertical ejection angle with prevailing winds distributing the finer explosion material southwestward. Elliott's Crater had a secondary directional blast to the south-southeast that produced a substantial hummocky breccia lobe.

Elliott's Crater was a hydrothermally active dome prior to its explosion, as recorded by bathymetry and seismic-reflection profiles. A significant seismic event at ca. 8 ka along the Eagle Bay fault zone ruptured the dome, triggering the large hydrothermal explosion. Large fragments of chlorite-rich clay from the dome cap rock are found in the lower explosion deposits and are inferred to be fragmented dome caprock. Similar deposits in mud slumps along the eastern shore of Yellowstone Lake suggest that sublacustrine mass movements may have been triggered by the seismic event that triggered the Elliott's Crater explosion or by the hydrothermal explosion itself.

The Mary Bay hydrothermal explosion is unique in its massive scale. We hypothesize that the Mary Bay explosion was triggered by several nearly synchronous events including the occurrences of a large seismic event (magnitude 6.5) at 13 ka along the 25-km-long Eagle Bay fault zone that produced a lake-wide tsunami. A sudden substantial ~14 m drop in Yellowstone Lake level is attributed to tsunami-related erosion of glacial material in the outlet channel of the Yellowstone River near LeHardy's Rapids. The attendant pressure decrease provided a powerful trigger for the huge Mary Bay hydrothermal explosion (Fig. 18). The energy release and volume of the explosion is estimated at four to six times that of the Elliott's Crater explosion.

Hydrothermal activity in Yellowstone Lake is long lived as evidenced by pervasively altered explosion debris and by active vent fields. The combination of high heat flow, frequent seismicity, and active deformation of the Yellowstone Caldera suggest that future hydrothermal explosions from Yellowstone Lake are a possibility and a potentially serious hazard.

ACKNOWLEDGMENTS

The sediment and gravity cores were collected under Yellowstone National Park (YNP) permits YELL-2016-SCI-7018 and YELL-2016-SCI-5054, YELL-2017-SCI-5054. Funding for this portion of the Hydrothermal Dynamics of Yellowstone Lake project was provided through National Science Foundation (NSF) Division of Earth Sciences grant numbers EAR 1515377 (University of Minnesota) and EAR 1515377 (University of Nebraska-Lincoln). Multibeam bathymetric mapping was conducted under permit YELL-2011-SCI-5054 and funded through the Jack and Richard Threet Chair in Sedimentary Geology at the University of Illinois at Urbana-Champaign. Coring at Cub Creek Pond was supported by NSF grant no. 1515353 and YELL-2017-SCI-0009. We are grateful for additional funding from the U.S. Geological Survey, The Global Foundation for Ocean Exploration, and the Yellowstone Foundation.We thank R. O'Grady, M. Shapley, M. Baker, D. Conley, and R. Sohn for expertise and assistance with Kullenberg coring; the engineers at The Global Foundation for Ocean Exploration; W. Inskeep and L. McKay for gravity coring; K.B. Shannon, A. Stone, M. Shapley, and others for assistance in the Continental Scientific Drilling Facility (University of Minnesota-Twin Cities, Minnesota); W. Lingwall and R. Brown at the Large Lake Observatory (University of Minnesota-Duluth); H. Kredit, A. Carlson, J. Seine, S. Haas, M. Mustafaga, D. Whaley, and rangers at YNP. We thank J. Lowenstern, M. Poland, R. Gresswell, and N. Heredia (U.S. Geological Survey), Maurice Tivey and Meg Tivey (Woods Hole Oceanographic Institute) and C. Bouligand (University of Grenoble). We thank R. Sohn and S. Mordensky for productive discussions, and J. Slack, B. Scheu, L. Mastin, and M. Clynne for constructive reviews. Any use of trade, firm, or product names is for descriptive purposes only and does not imply endorsement by the U.S. Government.

REFERENCES CITED

Aguilar, C., Cuhel, R.L., and Klump, J.V., 2002, Porewater and hydrothermal vent water inputs to Yellowstone Lake, Wyoming, *in* Anderson, R.J., and Harmon, D., eds., Yellowstone Lake: Hotbed of Chaos or Reservoir of Resilience: Proceedings of the 6th Biennial Scientific Conference on the Greater Yellowstone Ecosystem,

- National Park Service, Yellowstone National Park, p. 1–18.
- Balistrieri, L.S., Shanks, W.C., III, Cuhel, R.L., Aguilar, C., and Klump, J.V., 2007, The influence of sublacustrine hydrothermal vents on the geochemistry of Yellowstone Lake, in Morgan, L.A., ed., Integrated Geoscience Studies in the Greater Yellowstone Area: Volcanic, Hydrothermal, and Tectonic Processes in the Yellowstone Geoecosystem: U.S. Geological Survey Professional Paper 1717, p. 169–199, https://doi.org/1/10.3133/pp1717.
- Bargar, K.E., and Beeson, M.H., 1981, Hydrothermal alteration in research drill hole Y-2, Lower Geyser Basin, Yellowstone National Park, Wyoming: The American Mineralogist, v. 66, p. 473–490.
- Bennett, M.R., Doyle, P., and Mather, A.E., 1996, Dropstones: their origin and significance: Palaeogeography, Palaeoclimatology, and Palaeoecology, v. 121, p. 331– 339, https://doi.org/10.1016/0031-0182(95)00071-2.
- Bird, D.K., Schiffman, P., Elders, W.A., Williams, A.E., and McDowell, S.D., 1984, Calc-silicate mineralization in active geothermal systems: Economic Geology, v. 79, p. 671–695, https://doi.org/10.2113/gsecongeo.79 .4.671.
- Blinman, E., Mehringer, P.J., Jr., and Sheppard, J.C., 1979, Pollen influx and the deposition of Mazama and Glacier Peak tephra, in Sheets, P.D., and Grayson, D.K., eds., Volcanic Activity and Human Ecology: New York, USA, Academic Press, p. 393–425, https://doi.org/10 .1016/B978-0-12-639120-6.50018-2.
- Bouligand, C., Tivey, M.A., Finn, C.A., Morgan, L.A., Shanks, W.C.P., III, and Sohn, R.A., 2020, Geological and thermal control of the hydrothermal system in northern Yellowstone Lake: Inferences from highresolution magnetic surveys: Journal of Geophysical Research: Solid Earth, v. 125, no. 9, https://doi.org/10 .1029/2020JB019743.
- Brown, S.R., Cartier, R., Schiller, C.M., Zahajska, P., Fritz, S.C., Morgan, L.A., Whitlock, C., Conley, D.J., Lacey, J.H., Leng, M.J., and Shanks, W.C.P., III, 2021, Multi-proxy record of Holocene paleoenvironmental conditions from Yellowstone Lake, Wyoming, USA: Quaternary Science Reviews, v. 274, https://doi.org/10.1016/j.quascirev.2021.107275.
- Browne, P.R.L., and Lawless, J.V., 2001, Characteristics of hydrothermal eruptions, with examples from New Zealand and elsewhere: Earth-Science Reviews, v. 52, p. 299–331, https://doi.org/10.1016/S0012-8252(00)00030-1.
- Cash, R.W., 2015, Multibeam echosounding as a tool for mapping geologic features, bathymetry, and modern vents, Yellowstone National Park [M.S. thesis]: Urbana-Champaign, Illinois, USA, University of Illinois, 133 p.
- Chambefort, I., Lewis, B., Simpson, M.P., Bignall, G., Rae, A.J., and Ganefianto, N., 2017, Ngatamariki geothermal system: Magmatic to epithermal transition in the Taupo volcanic zone, New Zealand: Economic Geology, v. 112, p. 319–346, https://doi.org/10.2113/econgeo.112.2.319.
- Christiansen, R.L., 2001, The Quaternary and Pliocene Yellowstone Plateau volcanic field of Wyoming, Idaho, and Montana: U.S. Geological Survey Professional Paper 729-G, 145 p., https://doi.org/10.3133/pp729G.
- Christiansen, R.L., Lowenstern, J.B., Smith, R.B., Heasler, H., Morgan, L.A., Nathenson, M., Mastin, L.G., Muffler, L.J.P., and Robinson, J.E., 2007, Preliminary assessment of volcanic and hydrothermal hazards in Yellowstone National Park and vicinity: U.S. Geological Survey Open-File Report 2007-1071, 94 p., https:// doi.org/10.3133/ofr20071071.
- Day, S.J., 1996, Hydrothermal pore fluid pressure and the stability of porous, permeable volcanoes, in McGuire, W.J., Jones, A.P., and Neuberg, J., eds., Volcano Instability on the Earth and Other Planets: Geological Society of London, Special Publications, v. 110, p. 77–93, https://doi.org/10.1144/GSL.SP.1996.110.01.06.
- D'Elia, L., Paez, G., Hernando, I.R., Petrinovic, I.A., Lopez, L., Kurten, G., and Vigiani, L., 2020, Hydrothermal eruptions at El Humazo, Dumuyo geothermal field, Argentina: Insights into the eruptive dynamics and controls: Journal of Volcanology and Geothermal Research, v. 393, https://doi.org/10.1016/j.jvolgeores.2020.106786.

- De Vries, H.L., and Barendsen, G.W., 1954, Measurements of age by the carbon-14 technique: Nature, v. 174, no. 4442, p. 1138–1141, https://doi.org/10.1038/1741138a0.
- Dzurisin, D., Savage, J.C., and Fournier, R.O., 1990, Recent crustal subsidence at Yellowstone Caldera, Wyoming: Bulletin of Volcanology, v. 52, p. 247–270, https://doi.org/10.1007/BF00304098.
- Dzurisin, D., Yamashita, K.M., and Kleinman, J.W., 1994, Mechanisms of crustal uplift and subsidence at the Yellowstone Caldera, Wyoming: Bulletin of Volcanology, v. 56, p. 261–270, https://doi.org/10.1007/BF00302079.
- Dzurisin, D., Wicks, C.W., and Poland, M.P., 2012, History of surface displacements at the Yellowstone Caldera, Wyoming, from leveling surveys and InSAR observations, 1923–2008: U.S. Geological Survey Professional Paper 1788, 68 p., https://doi.org/10.3133/pp1788.
- Egan, J., Staff, R., and Blackford, J., 2015, A high-precision age estimate of the Holocene Plinian eruption of Mount Mazama, Oregon, USA: The Holocene, v. 25, p. 1054–1067, https://doi.org/10.1177/0959683615576230.
- Farrell, J., Smith, R.B., Husen, S., and Diehl, T., 2014, To-mography from 26 years of seismicity revealing that the spatial extent of the Yellowstone crustal magma reservoir extends well beyond the Yellowstone Caldera: Geophysical Research Letters, v. 41, p. 3068–3073, https://doi.org/10.1002/2014GL059588.
- Favorito, J.E., Harris, R.N., Sohn, R.A., Hurwitz, S., and Luttrell, K.M., 2021, Heat flux from a vapor-dominated hydrothermal field beneath Yellowstone Lake: Journal of Geophysical Research. Solid Earth, v. 126, no. 5, https://doi.org/10.1029/2020JB021098.
- Finn, C.A., and Morgan, L.A., 2002, High-resolution aeromagnetic mapping of volcanic terrain, Yellowstone National Park: Journal of Volcanology and Geothermal Research, v. 115, p. 207–231, https://doi.org/10.1016 /S0377-0273(01)00317-1.
- Fournier, R.O., 1989, Geochemistry and dynamics of the Yellowstone National Park hydrothermal system: Annual Review of Earth and Planetary Sciences, v. 17, p. 13–53, https://doi.org/10.1146/annurev.ea.17.050189 .000305.
- Fowler, A.P.G., Tan, C., Cino, C., Scheuermann, P., Volk, M.W.R., Shanks, W.C.P., III, and Seyfried, W.E., Jr., 2019a, Vapor-driven sublacustrine vents in Yellowstone Lake, Wyoming, USA: Geology, v. 47, p. 223–226, https://doi.org/10.1130/G45577.1.
- Fowler, A.P.G., Liu, Q.-l., Huang, Y., Tan, C., Volk, M.W.R., Shanks, W.C.P., III, and Seyfried, W., Jr., 2019b, Pyrite δ³⁴S and Δ³³S constraints on sulfur cycling at sublacustrine hydrothermal vents in Yellowstone Lake, Wyoming, USA: Geochimica et Cosmochimica Acta, v. 265, p. 148–162, https://doi.org/10.1016/j.gca.2019 .09.004.
- Fowler, A.P.G., Tan, C., Luttrell, K., Tudor, A., Scheuermann, P., Shanks, W.C.P., III, and Seyfried, W.E., Jr., 2019c, Geochemical heterogeneity of sublacustrine hydrothermal vents in Yellowstone Lake, Wyoming: Journal of Volcanology and Geothermal Research, v. 386, https:// doi.org/10.1016/j.jvolgeores.2019.106677.
- Gallagher, A., Montanaro, C., Cronin, S., Scott, B., Dingwell, D.B., and Scheu, B., 2020, Hydrothermal eruption dynamics reflecting vertical variations in host rock geology and geothermal alteration, Champagne Pool, Wai-o-tapu, New Zealand: Bulletin of Volcanology, v. 82, no. 77, https://doi.org/10.1007/s00445-020-01414-3.
- Gemery-Hill, P.A., Shanks, W.C., III, Balistrieri, L.S., and Lee, G.K., 2007, Geochemical data for selected rivers, lake waters, hydrothermal vents and subaerial geysers in Yellowstone National Park, Wyoming, and vicinity, 1996–2002, *in* Morgan, L.A., ed., Integrated Geoscience Studies in the Greater Yellowstone Area: Volcanic, Hydrothermal, and Tectonic Processes in the Yellowstone Geoecosystem: U.S. Geological Survey Professional Paper 1717, p. 365–426, https://doi.org/10.3133/pp1717.
- Goldhaber, M.B., 2003, Sulfur-rich sediments, in Holland, H.D., and Turekian, K.K., eds., Treatise on Geochemistry: Amsterdam, Netherlands, Elsevier Ltd., v. 7, p. 257–288, https://doi.org/10.1016/B0-08-043751-6 /07139-5.
- Heap, M.J., Baumann, T., Gilg, H.A., Kolzenburg, S., Ryan, A.G., Villeneuve, M., Russell, J.K., Kennedy, L.A.,

- Rosas-Carbajal, M., and Clynne, M.A., 2021, Hydrothermal alteration can result in pore pressurization and volcano instability: Geology, v. 49, https://doi.org/10.1130/G49063.1.
- Hurwitz, S., and Lowenstern, J.B., 2014, Dynamics of the Yellowstone hydrothermal system: Reviews of Geophysics, v. 52, p. 375–411, https://doi.org/10.1002 /2014RG000452.
- Jamtveit, B., Svensen, H., Podladchikov, Y., and Planke, S., 2004, Hydrothermal vent complexes associated with sill intrusions in sedimentary basins, in Breitkreuz, C., and Petford, N., eds., Physical geology of high-level magmatic systems: Geological Society of London Special Publication, v. 234, p. 233–241, https://doi.org/10 .1144/GSL.SP.2004.234.01.15.
- Jensen, B.J.L., and Beaudoin, A.B., 2016, Geochemical characterization of tephra deposits at archaeological and palaeoenvironmental sites across south-central Alberta and southwest Saskatchewan: Archaeological Survey of Alberta Occasional Paper, v. 36, p. 154–160.
- Johnson, S.Y., Stevenson, W.J., Morgan, L.A., Shanks, W.C., III, and Pierce, K.L., 2003, Hydrothermal and tectonic activity in northern Yellowstone Lake, Wyoming: Geological Society of America Bulletin, v. 115, p. 954–971, https://doi.org/10.1130/B25111.1.
- Kelts, K., Briegel, U., Ghilardi, K., and Hsu, K., 1986, The limnogeology-ETH coring system: Swiss Journal of Hydrology, v. 48, p. 104–115, https://doi.org/10.1007 /BF02544119.
- Kremer, K., Simpson, G., and Girardclos, S., 2012, Giant Lake Geneva tsunami in AD 563: Nature Geoscience, v. 5, p. 756–757, https://doi.org/10.1038/ngeo1618.
- Kremer, K., Anselmetti, F.S., Evers, F.M., Goff, J., and Nigg, V., 2021, Freshwater (paleo)tsunamis: A review: Earth-Science Reviews, v. 212, https://doi.org/10.1016/j.earscirev.2020.103447.
- Kuehn, S.C., Froese, D.G., Carrara, P.E., Foit, F.F., Pearce, N.J.G., and Rotheisler, P., 2009, Major- and traceelement characterization, expanded distribution, and a new chronology for the latest Pleistocene Glacier Peak tephras in western North America: Quaternary Research, v. 71, p. 201–216, https://doi.org/10.1016/j .yqres.2008.11.003.
- Licciardi, J.M., and Pierce, K.L., 2018, History and dynamics of the greater Yellowstone glacial system during the last two glaciations: Quaternary Science Reviews, v. 200, p. 1–33, https://doi.org/10.1016/j.quascirev.2018.08.027.
- Locke, W.W., Meyer, G.A., and Pings, J.C., 1992, Morphology of a postglacial fault scarp across the Yellowstone (Wyoming) caldera margin and its implications: Bulletin of the Seismological Society of America, v. 82, p. 511–516.
- Locke, W.W., and Meyer, G.A., 1994, A 12,000-year record of vertical deformation across the Yellowstone caldera margin: The shorelines of Yellowstone Lake: Journal of Geophysical Research. Solid Earth, v. 99, p. 20,079– 20,094, https://doi.org/10.1029/94JB00243.
- Lowenstern, J.B., Christiansen, R.L., Smith, R.B., Morgan, L.A., and Heasler, H., 2005, Steam explosions, earthquakes, and volcanic eruptions: What's in Yellowstone's future?: U.S. Geological Survey Fact Sheet 2005-3024, 6 p., https://doi.org/10.3133/fs20053024.
- Lu, Y., Fritz, S.C., Stone, J.R., Krause, T.R., Whitlock, C., Brown, E.T., and Benes, J.V., 2017, Trends in catchment processes and lake evolution during the late-glacial and early- to mid-Holocene inferred from high-resolution XRF data in the Yellowstone region: Journal of Paleolimnology, v. 58, p. 551–569, https://doi.org/10.1007 /s10933-017-9991-x.
- Mastin, L.G., 1991, The roles of magma and groundwater in the phreatic eruptions at Inyo Craters, Long Valley Caldera, California: Bulletin of Volcanology, v. 53, p. 579–596.
- Mastin, L.G., 1995, Thermodynamics of gas and steam-blast eruptions: Bulletin of Volcanology, v. 57, p. 85–98, https://doi.org/10.1007/BF00301399.
- Mastin, L.G., 2001, A simple calculator of ballistic trajectories for blocks ejected during volcanic eruptions: U.S. Geological Survey Open-File Report 2001-45, 18 p., https://doi.org/10.3133/ofr0145.
- Mastin, L.G., 2007, A user-friendly one-dimensional model for wet volcanic plumes: Geochemistry, Geophys-

- ics, Geosystems, v. 8, no. 3, https://doi.org/10.1029/2006GC001455.
- McKibbin, R., 1990, Mathematical modelling of hydrothermal eruptions, *in* 1990 International Symposium on Geothermal Energy: Geothermal Resources Council Transactions, v. 14, p. 1309–1316, https://www.geothermal-library.org/index.php?mode=pubs&action=view&record=1002040.
- McKibbin, R., Smith, T.A., and Fullard, L., 2009, Components and phases: Modelling progressive hydrothermal eruptions: The ANZIAM Journal, v. 50, p. 365–380, https://doi.org/10.1017/S144618110900011X.
- Mehringer, P.J., Blinman, E., and Petersen, K.L., 1977, Pollen influx and volcanic ash: Science, v. 198, p. 257–261, https://doi.org/10.1126/science.198.4314.257.
- Meyer, G.A., and Locke, W.W., 1986, Origin and deformation of Holocene shoreline terraces, Yellowstone Lake, Wyoming: Geology, v. 14, p. 699–702, https://doi.org/10.1130/0091-7613(1986)14<699:OADOHS>2.0.CO;2.
- Montanaro, C., Scheu, B., Cronin, S.J., Breard, E.C.P., Lube, G., and Dingwell, D.B., 2016a, Experimental estimates of the energy budget of hydrothermal eruptions; application to 2012 Upper Te Maari eruption, New Zealand: Earth and Planetary Science Letters, v. 452, p. 281–294, https://doi.org/10.1016/j.epsl.2016.07.052.
- Montanaro, C., Scheu, B., Gudmundsson, M.T., Vogfjord, K., Reynolds, H.I., During, T., Strehlow, K., Rott, S., Reuschle, T., and Dingwell, D.B., 2016b, Multidisciplinary constraints of hydrothermal explosions based on the 2013 Gengissig Lake events, Kverkfjoll Volcano, Iceland: Earth and Planetary Science Letters, v. 434, p. 308–319, https://doi.org/10.1016/j.epsl.2015.11.043.
- Montanaro, C., Cronin, S., Scheu, B., Kennedy, B., and Scott, B., 2020a, Complex crater fields formed by steamdriven eruptions: Lake Okaro, New Zealand: Geological Society of America Bulletin, v. 132, p. 1914–1930, https://doi.org/10.1130/B35276.1.
- Montanaro, C., Cronin, S.J., Scheu, B., Kennedy, B., Scott, B.J., and Dingwell, D.B., 2020b, Host rock variability powers the diversity of steam-driven eruptions: Geophysical Research Letters, v. 48, no.1, https://doi.org/ 1/10.1029/2020GL089025.
- Moore, J.G., Schweickert, R.A., and Kitts, C.A., 2014, Tsunami-generated sediment wave channels at Lake Tahoe, California-Nevada, USA: Geosphere, v. 10, p. 757–768, https://doi.org/10.1130/GES01025.1.
- Mordensky, S.P., Villeneuve, M.C., Kennedy, B.M., Heap, M.J., Gravley, D.M., Farquharson, J.I., and Reuschle, T., 2018, Physical and mechanical property relationships of a shallow intrusion and volcanic host rock, Pinnacle Ridge, Mt. Ruapehu, New Zealand: Journal of Volcanology and Geothermal Research, v. 359, p. 1–20, https://doi.org/10.1016/j.jvolgeores.2018.05.020.
- Morgan, L.A., Shanks, W.C., Lovalvo, D.A., Johnson, S.Y., Stephenson, W.J., Pierce, K.L., Harlan, S.S., Finn, C.A., Lee, G., Webring, M., Schulze, B., Duehn, J., Sweeney, R.E., and Balistrieri, L.S., 2003, Exploration and discovery in Yellowstone Lake: Results from high-resolution sonar imaging, seismic reflection profiling, and submersible studies: Journal of Volcanology and Geothermal Research, v. 122, p. 221–242, https://doi.org/10.1016/S0377-0273(02)00503-6.
- Morgan, L.A., Shanks, W.C., III, Lee, G.K., and Webring, M.W., 2007a, Bathymetry and geology of the floor of Yellowstone Lake, Yellowstone National Park, Wyoming, Idaho, and Montana: U.S. Geological Survey Scientific Investigations Map 2973, 2 plates, scale 1:76,821, https://doi.org/10.3133/sim2973.
- Morgan, L.A., Shanks, W.C., III, Pierce, K.L., Lovalvo, D.A., Lee, G.K., Webring, M.W., Stephenson, W.J., Johnson, S.Y., Harlan, S.S., Schulze, B., and Finn, C.A., 2007b, The floor of Yellowstone Lake is anything but quiet: New discoveries from high-resolution sonar imaging, seismic-reflections profiling, and submersible studies, in Morgan, L.A., ed., Integrated Geoscience Studies in the Greater Yellowstone Area: Volcanic, Hydrothermal, and Tectonic Processes in the Yellowstone Geoecosystem: U.S. Geological Survey Professional Paper 1717, p. 91–126, https://doi.org/10.3133/pp1717.
- Morgan, L.A., Shanks, W.C.P., III, and Pierce, K.L., 2009, Hydrothermal processes above the Yellowstone magma chamber: Large hydrothermal systems and large hydro-

- thermal explosions: Geological Society of America Special Paper 459, 95 p., https://doi.org/10.1130/SPE459.
- Morgan, P., Blackwell, D.D., Spafford, R.E., and Smith, R.B., 1977, Heat flow measurements in Yellowstone Lake and the thermal structure of the Yellowstone Caldera: Journal of Geophysical Research. Solid Earth, v. 82, p. 3719–3732, https://doi.org/10.1029/ //JB082i026p03719.
- Muffler, L.P.J., White, D.E., and Truesdell, A.H., 1971, Hydrothermal explosion craters in Yellowstone National Park: Geological Society of America Bulletin, v. 82, p. 723–740, https://doi.org/10.1130 //0016-7606(1971)82[723:HECIYN]2.0.CO;2.
- Nigg, V., Wohlwend, S., Hilbe, M., Bellwald, B., Fabbri, S.C., de Souza, G.F., Donau, F., Grischott, R., Strasser, M., and Anselmetti, F.S., 2021, A tsunamigenic delta collapse and its associated tsunami deposits in and around Lake Sils, Switzerland: Natural Hazards, v. 107, p. 1069–1103, https://doi.org/10.1007/s11069-021-04533-v.
- Norris, P.W., 1881, Fifth Annual Report of the Superintendent of the Yellowstone National Park: Washington, D.C., U.S. Government Printing Office, 94 p., https://www.archive.org/details/annualreportofsu1881unit.
- Otis, R.M., Smith, R.B., and Wold, R.J., 1977, Geophysical surveys of Yellowstone Lake: Journal of Geophysical Research, Solid Earth, v. 82, p.3705-3717, https://doi.org.10.1029/JB082i026p03705.
- Passaro, S., Tamburrino, S., Vallefuoco, M., Gherardi, S., Sacchi, M., and Ventura, G., 2016, High-resolution morpho-bathymetry of the Gulf of Naples, eastern Tyrrhenian Sea: Journal of Maps, v. 12, p. 203–210, https:// doi.org/10.1080/17445647.2016.1191385.
- Phillips-Lander, C.M., Fowle, D.A., Taunton, A., Hernandez, W., Mora, M., Moore, D., Shinogle, H., and Roberts, J.A., 2014, Silicate dissolution in Las Pailas thermal field: Implications for microbial weathering in acidic volcanic hydrothermal spring systems: Geomicrobiology Journal, v. 31, p. 23–41, https://doi.org/10.1080/01490451.2013.802395.
- Pickrill, R.A., 1993, Shallow seismic stratigraphy and pock-marks of a hydrothermally influenced lake, Lake Rotoiti, New Zealand: Sedimentology, v. 40, p. 813–828, https://doi.org/10.1111/j.1365-3091.1993.tb01363.x.
- Pierce, K.L., Cannon, K.L., Meyer, G.A., Trebesch, M.J., and Watts, R.D., 2007, Postglacial inflation-deflation cycles, tilting, and faulting in the Yellowstone Caldera based on Yellowstone Lake shorelines, in Morgan, L.A., ed., Integrated Geoscience Studies in the Greater Yellowstone Area: Volcanic, Hydrothermal, and Tectonic Processes in the Yellowstone Geoecosystem: U.S. Geological Survey Professional Paper 1717, p. 127–168, https://doi.org/10.3133/pp1717.
- Reimer, P.J., Bard, E., Bayliss, A., Beck, J.W., Blackwell, P.G., Ramsey, C.B., Buck, C.E., Cheng, H., Edwards, R.L., Friedrich, M., Grootes, P.M., Guilderson, T.P., Haflidason, H., Hajdas, I., Kaiser, K.F., Kromer, B., Manning, S.W., Niu, M., Reimer, R.W., Richards, D.A., Scott, E.M., Southon, J.R., Staff, R.A., Turney, C.S.M., and van der Plicht, J., 2013, IntCal13 and Marine13 radiocarbon age calibration curves 0–50,000 Years cal BP: Radiocarbon, v. 55, p. 1869–1887, https://doi.org/10.2458/azu_js_rc.55.16947.
- Richmond, G.M., 1973, Surficial geologic map of the West Thumb quadrangle, Yellowstone National Park, WY: U.S. Geological Survey Miscellaneous Geologic Investigations Map I-643, scale 1:62,500, 1 plate.
- Richmond, G.M., 1976, Surficial geologic history of the Canyon Village quadrangle, Yellowstone National Park, Wyoming, for use with Map I-652: U.S. Geological Survey Bulletin 1427, 35 p., https://doi.org/10.3133 /h1427
- Richmond, G.M., 1977, Surficial geologic map of the Canyon Village quadrangle, Yellowstone National Park, WY: U.S. Geological Survey Miscellaneous Geologic Investigations Map I-652, scale 1:62,500, 1 plate, https://doi.org/10.3133/i652.
- Rye, R.O., and Truesdell, A.H., 2007, The question of recharge to the deep thermal reservoir underlying the geysers and hot springs of Yellowstone National Park, in Morgan, L.A., ed., Integrated Geoscience Studies in the Greater Yellowstone Area: Volcanic, Hydrothermal, and Tectonic Processes in the Yellowstone Geoecosys-

- tem: U.S. Geological Survey Professional Paper 1717, p. 235–270, https://doi.org/10.3133/pp1717.
- Schiller, C.M., Alt, M., Whitlock, C., and Morgan, L.A., 2020, Vegetation responses to Quaternary volcanic and hydrothermal disturbances in the northern Rocky Mountains and greater Yellowstone ecosystem (USA): Palaeogeography, Palaeoclimatology, Palaeoecology, v. 559, https://doi.org/10.1016/j.palaeo.2020.109859.
- Schiller, C.M., Whitlock, C., Elder, K.L., Iverson, N.A., and Abbott, M.B., 2021, Erroneously old radiocarbon ages from terrestrial pollen concentrates in Yellowstone Lake, Wyoming, USA: Radiocarbon, v. 63, p. 321–342, https://doi.org/10.1017/RDC.2020.118.
- Shanks, W.C., III, Morgan, L.A., Balistrieri, L., and Alt, J.C., 2005, Hydrothermal vent fluids, siliceous hydrothermal deposits, and hydrothermally altered sediments in Yellowstone Lake, in Inskeep, W.P., and McDermott, T.R., eds., Geothermal Biology and Geochemistry in Yellowstone National Park: Bozeman, Montana, USA, Thermal Biology Institute, p. 53–72.
- Shanks, W.C., III, Alt, J.C., and Morgan, L.A., 2007, Geochemistry of sublacustrine hydrothermal deposits in Yellowstone Lake: Hydrothermal reactions, stable-isotope systematics, sinter deposition, and spire growth, in Morgan, L.A., ed., Integrated Geoscience Studies in the Greater Yellowstone Area: Volcanic, Hydrothermal, and Tectonic Processes in the Yellowstone Geoecosystem: U.S. Geological Survey Professional Paper 1717, p. 201–234, https://doi.org/10.3133/pp1717.
- Shanks, W.C., Morgan, L.A., Benzel, W.M., Mills, C.T., Moscati, R.J., 2019, Geochemistry of hydrothermally altered sediments, pore fluids, and hydrothermal explosion deposits from Yellowstone Lake: V33D-0207 Abstract presented at 2019 Fall Meeting, AGU, San Francisco, California, 9–13 December.
- Sherrod, B.L., 1989, Paleolimnology of Alder Lake and its implications for Holocene tectonics in Yellowstone National Park, Wyoming [M.S. thesis]: Pittsburgh, Pennsylvania, University of Pittsburgh.

- Smith, R.B., Jordan, M., Steinberger, B., Puskas, C.M., Farrell, J., Waite, G.P., Husen, S., Chang, W.L., and O'Connell, R., 2009, Geodynamics of the Yellowstone hotspot and mantle plume: Seismic and GPS imaging, kinematics, and mantle flow: Journal of Volcanology and Geothermal Research, v. 188, p. 26–56, https://doi.org/10.1016/j.jvolgeores.2009 .08.020.
- Smith, T., and McKibbin, R., 2000, An investigation of boiling processes in hydrothermal eruptions, in Proceedings of the World Geothermal Congress, Kyushu, Japan, May 28–June 10, 2000: Auckland, New Zealand, International Geothermal Association, v. 1, p. 699–704, www.geothermal-energy.org/pdf/IGAstandard/WGC /2000/R0133.PDF.
- Smoot, J.P., Litwin, R.J., Bischoff, J.L., and Lund, S.J., 2000, Sedimentary record of the 1872 earthquake and "tsunami" at Owens Lake, southeast California: Sedimentary Geology, v. 135, p. 241–254, https://doi.org/10.1016 /S0037-0738(00)00075-0.
- Sohn, R., Harris, R., Linder, C., Luttrell, K., Lovalvo, D., Morgan, L., Seyfried, W., and Shanks, P., 2017, Exploring the restless floor of Yellowstone Lake: Eos, v. 98, https://doi.org/10.1029/2017EO087035.
- Sohn, R.A., Luttrell, K., Shroyer, E., Stranne, C., Harris, R.N., and Favorito, J.E., 2019, Observations and modeling of a hydrothermal plume in Yellowstone Lake: Geophysical Research Letters, v. 46, p. 6435–6442, https://doi.org/10.1029/2019GL082523.
- Strasser, M., Schindler, C., and Anselmetti, F.S., 2008, Late Pleistocene earthquake-triggered moraine dam failure and outburst of Lake Zurich, Switzerland: Journal of Geophysical Research. Earth Surface, v. 113, no. F2, https://doi.org/10.1029/2007JF000802.
- Stuiver, M., Reimer, P.J., and Reimer, R.W., 2020, CALIB 7.1: http://calib.org (accessed 19 February 2020).
- Theriot, E.C., Fritz, S.C., Whitlock, C., and Conley, D.J., 2006, Late Quaternary rapid morphological evolution of an endemic diatom in Yellowstone Lake, Wyoming:

- Paleobiology, v. 32, p. 38–54, https://doi.org/10.1666/0094-8373(2006)032[0038:LQRMEO]2.0.CO;2.
- Tiller, C.C., 1995, Postglacial sediment stratigraphy of large lakes in greater Yellowstone: Scenarios of tectonic and climatic forcing [M.S. thesis]: Minneapolis, University of Minnesota, Twin Cities, 193 p.
- Truesdell, A.H., Nathenson, M., and Rye, R.O., 1977, The effect of subsurface boiling and dilution on the isotopic compositions of the Yellowstone thermal waters: Journal of Geophysical Research, v. 82, p. 3694–3704, https://doi.org/10.1029/JB082i026p03694.
- Velbel, M.A., 2007, Surface textures and dissolution processes of heavy minerals in the sedimentary cycle: Examples from pyroxenes and amphiboles: Developments in Sedimentology, v. 58, p. 113–150, https://doi.org/10.1016/S0070-4571(07)58004-0.
- Wells, D.L., and Coppersmith, K.J., 1994, New empirical relationships among magnitude, rupture length, rupture width, rupture area, and surface displacements: Bulletin of the Seismological Society of America, v. 84, p. 974–1004.
- Wicks, C.W., Thatcher, W., Dzurisin, D., and Svarc, J., 2006, Uplift, thermal unrest and magma intrusion at Yellowstone Caldera: Nature, v. 440, p. 72–75, https://doi.org /10.1038/nature04507.
- Wold, R.J., Mayhew, M.A., and Smith, R.B., 1977, Bathymetric and geophysical evidence for a hydrothermal explosion crater in Mary Bay, Yellowstone Lake, Wyoming: Journal of Geophysical Research. Solid Earth, v. 82, p. 3733–3738, https://doi.org/10.1029/JB082i026p03733.

SCIENCE EDITOR: WENJIAO XIAO ASSOCIATE EDITOR: NANCY RIGGS

Manuscript Received 14 May 2021 Revised Manuscript Received 1 February 2022 Manuscript Accepted 13 March 2022

Printed in the USA